

# Shape optimization of phononic band gap structures using the homogenization approach

Jaroslav Vondřejc<sup>\*1</sup>, Eduard Rohan<sup>†2</sup>, and Jan Heczko<sup>‡2</sup>

<sup>1</sup>Institute of Scientific Computing, Technische Universität Braunschweig,  
Mühlenpfordstrasse 23, 38106 Braunschweig, Germany.

<sup>2</sup>European Centre of Excellence, NTIS – New Technologies for Information Society Faculty  
of Applied Sciences, University of West Bohemia, Univerzitní 22, 30614 Pilsen, Czech  
Republic

## Abstract

The paper deals with optimization of the acoustic band gaps computed using the homogenized model of strongly heterogeneous elastic composite which is constituted by soft inclusions periodically distributed in stiff elastic matrix. We employ the homogenized model of such medium to compute intervals — band gaps — of the incident wave frequencies for which acoustic waves cannot propagate. It was demonstrated that the band gaps distribution can be influenced by changing the shape of inclusions. Therefore, we deal with the shape optimization problem to maximize low-frequency band gaps; their bounds are determined by analyzing the effective mass tensor of the homogenized medium. Analytic transformation formulas are derived which describe dispersion effects of resizing the inclusions. The core of the problem lies in sensitivity of the eigenvalue problem associated with the microstructure. Computational sensitivity analysis is developed, which allows for efficient using of the gradient based optimization methods. Numerical examples with 2D structures are reported to illustrate the effects of optimization with stiffness constraint. This study is aimed to develop modeling tools which can be used in optimal design of new acoustic devices for “smart systems”.

**Keywords:** phononic materials, band gap structures, optimization, sensitivity analysis, homogenization

## 1 Introduction

Phononic materials, often called phononic crystals [22], are elastic composites with periodic structure and with large contrasts in elasticity of the constituents. For certain frequency ranges called *band gaps*, such elastic structures can effectively attenuate propagation of incident acoustic waves, see *e.g.* [18, 43] where this property has been studied experimentally. Due to this behavior, the phononic materials may be used in modern technologies to generate frequency filters, as beam splitters, sound or vibration protection devices (for noise reduction), or they may serve as waveguides.

It has been noted as early as in eighties of the last century, cf. [2], see the reviews [29, 3], that constitutive relationships of the elastodynamics are non-local in space and time and that the

---

<sup>\*</sup>E-mail: vondrejcz@gmail.com

<sup>†</sup>E-mail: rohan@kme.zcu.cz

<sup>‡</sup>E-mail: jheczko@ntis.zcu.cz

*effective inertia mass* presents, in general, an anisotropic second order tensor which depends on the frequency of imposed oscillations, or incident waves. Due to this property, the wave dispersion may become very strong for frequencies in whole bands – *band gaps* – where the effective (homogenized) inertia mass becomes indefinite, or even negative definite, such that the elastic composites may *lose their potential capability to behave as harmonic oscillators*<sup>1</sup>.

## 1.1 Modelling of the phononic materials and band gap analysis

The classical continuum approach to the band gap analysis, also frequently reported in the literature in the context of the material optimization, *e.g.* [44, 12, 25, 11, 19], is based on the Bloch-Floquet theory for waves in an unbounded medium. This treatment requires that the band gaps are searched for specified wave directions on the boundary of the first Brillouin zone.

An alternative and effective way of modeling the phononic materials, which is also adhered to in this paper, is based on the asymptotic homogenization method applied to the strongly heterogeneous elastic [2, 4], or piezoelectric medium [34, 35, 7]. This approach was first developed to study effective behavior of the *photonic crystals* used in optical devices, cf. [49, 9, 26]. In [5], the scaling ansatz for periodically oscillating coefficients of the scalar Helmholtz equation governing the electromagnetic wave propagation was proposed, such that the band gaps could be analyzed according to the sign of the effective coefficient. The idea was extended to elasticity due to similarity of the mathematical description, although the band gap analysis becomes more complex with respect to the wave polarization [4], cf. [38]. The same mathematical tools were used in [42] to treat strongly anisotropic elastic structures, so that effective band gaps are relative to the wave polarization and the direction of propagation. It is worth to note, that higher-order homogenization theory is now being developed to respect transition effects which are not captured by the first order theory, see *e.g.* [32]. Beyond the classical continuum theory, the relaxed micromorphic continua serve a good basis for studying acoustic wave dispersion and band gaps [24].

We consider periodically heterogeneous elastic composites with the characteristic size of the heterogeneities proportional to  $\varepsilon$ ; this small parameter also determines the size of the so-called *representative periodic cell* (RPC). Although, in general, the material properties may vary arbitrarily in the RPC, we confine to materials where the RPC is formed by an elastic matrix and a very soft inclusion with the shape, which influences the effective medium properties. The medium is subject to a periodic excitation. The limit homogenized model, obtained by the asymptotic analysis with  $\varepsilon \rightarrow 0$ , describes acoustic wave propagation in the effective elastic medium and is characterized by the homogenized elastic fourth order tensor and by the homogenized second order mass tensor. By designing the shape of the "soft" inclusions in the RPC, we can manipulate the range of frequencies for which this homogenized *mass tensor becomes negative* w.r.t. waves of some polarizations so that, as the consequence, those waves cannot propagate. It has been shown in [38] that analysis of the eigenvalues of the mass tensor is sufficient to identify the band gaps independently of the direction of the wave propagation. Therefore, the band gaps can be optimized without any need to evaluate the Brillouin zone.

Although in this paper we focus on the elastic composites, an extension for *piezoelectric composite materials* is possible following the same approach, see *e.g.* [34] where the associated modifications concerning the homogenized model and the sensitivity analysis were discussed. In these materials, besides the passively controlled band gaps by designing microstructure-related geometrical param-

---

<sup>1</sup>The notion of band gaps is introduced as the range of frequencies for which the structure is blocked from free vibrations. However, as we shall see below, the definition of the band gaps requires more complexity in order to respect the material anisotropy.

eters, see [27, 28], alternatively the *piezo-phononic* structures can also be controlled “actively” by external electrical fields, due to the electro-mechanical coupling.

## 1.2 Optimal design of the band gap structures

Optimization of *band gap structures*, or phononic crystals enjoys increasing attention over the last decade. The topic is challenging owing to the wide applicability of the metamaterials featured by the band gap property. Moreover, new technologies like 3D printing show new perspectives in the optimal metamaterial design based on computational analysis. There is a vast body of literature devoted to the phononic material optimization, see *e.g.* [41, 10, 21, 13, 50, 48, 30]. Typically, the optimization merit is to modify widths of the band gap intervals. The design parameters are related to the shape of one or more inclusions situated in the RPC, as in our case, or to the microstructure topology. The topology optimization of the phononic crystals within the classical Bloch-Floquet theory was first treated by Sigmund and Jensen in [41], where also the global problem in a finite domain was considered. Recently, using the same framework, the topology optimization was extended for the piezo-phononic structures in [44].

Although, in general, the topology optimization, *e.g.* [40], leads to better designs than the shape optimization with a fixed topology, the latter approach is of pertaining interest. From the practical point of view, it leads to metamaterial designs which can be manufactured relatively easier than quite general designs arising from the topology optimization. Moreover, it was pointed out by Milton and Willis [29], that the band gap property depends on the size and the shape of inclusions, however, it is insensitive to deviations from their exactly periodic distribution. This observation is coherent with the homogenization result and the related band gap definition employed in this paper, *cf.* [38]. In this context, responses of locally resonant acoustic metamaterials designed as rubber-coated hard particles in a compliant matrix (*cf.* [6]) were studied in [21], where the same phenomenon of insensitivity of the band gaps *w.r.t.* periodic placements of the particles was shown. From the theoretical point of view, it is not yet understood, how the inclusion shape can contribute to the band gap widening while design constraints are imposed to control the material stiffness. The present paper should give answers related to this issue.

In this paper, we rely on the homogenization approach [4, 38] of modeling phononic materials in 2D under the plane strain condition; alternatively the plane stress condition can be prescribed, so that the 2D problem can describe the in-plane waves in plates (the homogenized phononic plates were introduced in [37, 36], and elaborated further in [33]). The optimal shape problem is formulated for a single “soft” elastic inclusion embedded in the matrix of the RPC. The shape is described by the circular B-spline which ensures enough regularity independently of the numerical discretization. The constraints are related to the effective stiffness of the composite. Besides solving the optimal design problem, we explore dependence of the band gap distribution on the volume fraction of the soft phase, *i.e.* on size of the inclusion.

The plan of the paper is as follows. In Section 2 we introduce the mathematical model of the homogenized phononic material and explain the band gap analysis based on the effective mass tensor. The effects related to the change of RPC size and the inclusion size are discussed in Section 3, where rescaling formulas are given; it enables to transform the band gaps distribution accordingly. The optimal shape problem is formulated in Section 4, followed by the sensitivity analysis in Section 5, where the computation of the total gradients of the band gap bounds *w.r.t.* the design variables are introduced. Numerical algorithms are summarized in Section 6, where also some selected examples of solved problems are reported. As initial designs, we consider the square-shaped and L-shaped inclusions; it is shown, how maximization of the first and the second band gap leads to

different optimal shapes. In the conclusion, we summarize the particular amendments of the paper, and comment on some particular issues which will be handled in a future work. Some technical contributions of the paper are postponed in the Appendix.

## 2 Problem setting

An elastic composite with a periodic structure is featured by the characteristic size<sup>2</sup>  $\varepsilon = \ell/L$ . This is the ratio between the diameter  $\ell$  of a generating representative cell and a “macroscopic” length  $L$  corresponding to the wavelength of propagating waves, or to the size of the an open bounded domain  $\Omega \subset \mathbb{R}^d$ ,  $d = 2, 3$  occupied by the composite. It is constituted by two different materials: the one occupying the domain  $\Omega_1^\varepsilon$  called *the matrix* and the other one situated in the domain  $\Omega_2^\varepsilon$  called *the inclusions*. Importantly, we shall assume that domain  $\Omega_1^\varepsilon$  is connected. The material constituents vary periodically with the local position.

Throughout the text all the quantities varying with this microstructural periodicity are labeled with superscript  $^\varepsilon$ . We use the usual boldface notation to denote the vectors  $\mathbf{a} = (a_i)$  or the 2nd order tensors  $\mathbf{B} = (B_{ij})$  for  $i, j = 1, \dots, d$ .

The following functional spaces are used: by  $L^2(D)$  we refer to square integrable functions defined in an open bounded domain  $D$ ; by  $H^1(D)$  we mean the Sobolev space  $W^{1,2}(D) \subset L^2(D)$  composed of square integrable functions including their first generalized derivatives; space  $H_0^1(D) \subset H^1(D)$  is constituted by functions with zero trace on  $\partial D$ . Bold notation is used to denote spaces of vector-valued functions, *e.g.*  $\mathbf{H}^1(D)$ . We shall consider periodic functions defined in special domains  $Y = ]0, 1[^d \subset \mathbb{R}^d$ , where  $d = 2, 3$ ; we shall need spaces of  $Y$ -periodic functions, labelled by subscript  $\#$ , thus,  $\mathbf{H}_\#^1(Y)$  contains functions  $\mathbf{f} \in \mathbf{H}^1(Y)$  extended by  $Y$ -periodicity from  $Y$  to  $\mathbb{R}^d$  using  $\mathbf{f}(y') = \mathbf{f}(y)$  with  $y' = y + k$  for any  $k \in \mathbb{Z}^d$ .

### 2.1 Heterogeneous elastic structure

The material properties are associated to the periodic geometrical decomposition which is now introduced. We consider the *reference (unit) cell*  $Y = ]0, 1[^d$  which generate the structure as the periodic lattice. The cell consists of an inclusion  $\overline{Y}_2 \subset Y$ , embedded in the matrix part  $Y_1 = Y \setminus \overline{Y}_2$  so that the interface  $\Gamma = \partial Y_2$  is contained in  $Y$ . In general, cell  $Y$  may be defined as a parallelepiped, the particular choice of the unit cube in  $\mathbb{R}^d$  is used just for an ease of explanation; we shall return to this issue in Remark 4. Using the reference cell we generate the decomposition of  $\Omega$  as the union of all inclusions (which should not penetrate boundary  $\partial\Omega$ ), having the size  $\approx \varepsilon$ ,

$$\Omega_2^\varepsilon = \bigcup_{k \in \mathbb{K}^\varepsilon} \varepsilon(Y_2 + k), \text{ where } \mathbb{K}^\varepsilon = \{k \in \mathbb{Z} \mid \varepsilon(k + \overline{Y}_2) \subset \Omega\}, \quad (1)$$

whereas the perforated matrix is  $\Omega_1^\varepsilon = \Omega \setminus \Omega_2^\varepsilon$ . Also we introduce the interface  $\Gamma^\varepsilon = \overline{\Omega_1^\varepsilon} \cap \overline{\Omega_2^\varepsilon}$ , so that  $\Omega = \Omega_1^\varepsilon \cup \Omega_2^\varepsilon \cup \Gamma^\varepsilon$ .

Properties of a three dimensional body made of the elastic material are described by the elasticity tensor  $\mathbf{C}^\varepsilon = (C_{ijkl})^\varepsilon$ , where  $i, j, k = 1, 2, \dots, d$ . As usually we assume both major and minor symmetries of  $C_{ijkl}^\varepsilon$  (*i.e.*  $C_{ijkl}^\varepsilon = C_{klij}^\varepsilon = C_{jikl}^\varepsilon$ ), and the ellipticity,

We assume that inclusions are occupied by a “very soft material” in such a sense that coefficients of *the elasticity tensor in the inclusions* are significantly smaller than those of the matrix compartment, however *the material density* is comparable in both the compartments. The physical

---

<sup>2</sup>The so-called characteristic size of the “microstructure”.

aspects of such an arrangement of the periodic structure has been discussed *e.g.* in [38]; the soft inclusions behave as passive dampers inducing an anti-resonance effect for certain frequencies, as explained in Section 2.4.

The material parameters are defined with respect to the decomposition of generating cell  $Y$ , as follows:

$$\rho^\varepsilon(x) = \begin{cases} \rho^1(y) & \text{for } y \in Y_1, \\ \rho^2(y) & \text{for } y \in Y_2, \end{cases} \quad C_{ijkl}^\varepsilon(x) = \begin{cases} C_{ijkl}^1(y) & \text{for } y \in Y_1, \\ C_{ijkl}^{2,\varepsilon}(y) = \varepsilon^2 \bar{C}_{ijkl}^2(y) & \text{for } y \in Y_2, \end{cases} \quad (2)$$

where, by virtue of the decomposition introduced in (1), see *e.g.* [8],  $y := \{x/\varepsilon\}_Y$  is the local “microscopic” coordinate associated with the global “macroscopic” position  $x \in \Omega$ . As an important feature of the modeling based on the asymptotic analysis, the *strong heterogeneity* in the elastic coefficients is related to the geometrical scale  $\varepsilon$  of the underlying microstructure by the coefficient  $\varepsilon^2$ . Due to this scaling an internal scale of the structure is retained when passing to the limit  $\varepsilon \rightarrow 0$  and the homogenized model exhibits dispersive behaviour; this phenomenon cannot be observed when standard two-scale homogenization procedure is applied to a medium with scale-independent material parameters, cf. [2].

**Remark 1.** The limit homogenized model of the strongly heterogeneous medium can be used to describe real situation only for a given scale, *i.e.* for a given  $\varepsilon > 0$ , such that  $\varepsilon Y = ]0, \varepsilon]^2$  is the actual *real-sized reference cell*. In fact, the elasticity  $\varepsilon^2 \bar{\mathbf{C}}^2$  corresponds to the physical values of the elasticity tensor, so that, due to (2), the elasticity  $\mathbf{C}^{\text{phys}}$  of a given real material situated in the inclusions  $\Omega_2^\varepsilon$  is related to the model coefficients  $\bar{\mathbf{C}}^2$  by the following relationship:  $\mathbf{C}^{\text{phys}}(x) \equiv \mathbf{C}^\varepsilon(x) = \varepsilon^2 \bar{\mathbf{C}}^2(y)$  for  $y = \{x/\varepsilon\}_Y \in Y_2$ . To derive the limit model using the asymptotic analysis, when  $\varepsilon \rightarrow 0$ ,  $\bar{\mathbf{C}}^2$  is treated as a fixed parameter.

△

## 2.2 Modeling the stationary waves

We consider stationary wave propagation in the medium introduced above. Although the problem can be treated for a general case of boundary conditions, for simplicity we restrict the model to the description of clamped structures loaded by volume forces. Assuming a harmonic single-frequency volume forces,

$$\mathbf{F}(x, t) = \mathbf{f}(x) e^{i\omega t},$$

where  $\mathbf{f} = (f_i)$ ,  $i = 1, \dots, d$  is its local amplitude and  $\omega$  is the frequency,  $i^2 = -1$ . We consider a dispersive displacement field with the local magnitude  $\mathbf{u}^\varepsilon$

$$\mathbf{U}^\varepsilon(x, \omega, t) = \mathbf{u}^\varepsilon(x, \omega) e^{i\omega t},$$

This allows us to study the steady periodic response of the medium, as characterized by displacement field  $\mathbf{u}^\varepsilon$  which satisfies the following boundary value problem:

$$-\omega^2 \rho^\varepsilon \mathbf{u}^\varepsilon - \operatorname{div} \boldsymbol{\sigma}^\varepsilon = \mathbf{f} \quad \text{in } \Omega, \quad \mathbf{u}^\varepsilon = 0 \quad \text{on } \partial\Omega, \quad (3)$$

where the stress tensor  $\boldsymbol{\sigma}^\varepsilon = (\sigma_{ij}^\varepsilon)$  is expressed by the Hooke's law  $\boldsymbol{\sigma}^\varepsilon = \mathbf{C}\mathbf{e}^\varepsilon$  involving the linearized strain tensor  $\mathbf{e}^\varepsilon = (e_{ij}^\varepsilon)$  which for a displacement field  $\mathbf{v} = (v_i)$  is given by  $e_{ij}^\varepsilon(\mathbf{v}) = 1/2(\partial_j v_i + \partial_i v_j)$ . The problem (3) can be formulated in a weak form as follows: Find  $\mathbf{u}^\varepsilon \in \mathbf{H}_0^1(\Omega)$ , such that

$$-\omega^2 \int_{\Omega} \rho^\varepsilon \mathbf{u}^\varepsilon \cdot \mathbf{v} + \int_{\Omega} [\mathbf{C}^\varepsilon \mathbf{e}(\mathbf{u}^\varepsilon)] : \mathbf{e}(\mathbf{v}) = \int_{\Omega} \mathbf{f} \cdot \mathbf{v} \quad \text{for all } \mathbf{v} \in \mathbf{H}_0^1(\Omega),$$

where  $\mathbf{H}_0^1(\Omega)$  is the standard Sobolev space of vectorial functions with square integrable generalized derivatives and with vanishing trace on  $\partial\Omega$ , as required by (3)<sub>2</sub>.

### 2.3 Homogenized model

Methods of homogenization are widely accepted as modeling tool which allows to associate a medium with some heterogeneous microstructure with a homogeneous model relevant to the macroscopic scale. In [4], the unfolding operator method of homogenization [8] was applied with the strong heterogeneity assumption (2); it can be shown that there is a limit macroscopic displacement field  $\bar{\mathbf{u}}$  which satisfies the equation of the homogenized medium; in fact for  $\varepsilon \rightarrow 0$ ,  $\mathbf{u}^\varepsilon$  converges weakly to the macroscopic displacement field  $\mathbf{u}$  with perturbations localized in the inclusions. These local perturbations are related to  $\mathbf{u}$  by characteristic responses introduced below. They give rise to a correction term of the “effective” mass coefficients which is responsible for the wave dispersion and the band gap effect, in particular. We shall now record the resulting system of coupled equations, as derived in [4], which describe the structure behavior at two scales, the *macroscopic* one and the *microscopic* one.

First we define the *homogenized coefficients*<sup>3</sup> involved in the homogenized model of wave propagation. The “frequency-dependent coefficients” are determined just by material properties of the inclusion and by the material density  $\rho^1$ , whereas the elasticity coefficients are related exclusively to the matrix material occupying the perforated domain.

*Frequency-dependent homogenized coefficients* involved in the macroscopic momentum equation are expressed in terms of eigenelements  $(\lambda^r, \boldsymbol{\varphi}^r) \in \mathbb{R} \times \mathbf{H}_0^1(Y_2)$ ,  $r = 1, 2, \dots$  of the elastic spectral problem which is imposed in inclusion  $Y_2$  with  $\boldsymbol{\varphi}^r = 0$  on  $\partial Y_2$ :

$$\int_{Y_2} [\bar{\mathbf{C}}^2 \mathbf{e}^y(\boldsymbol{\varphi}^r)] : \mathbf{e}^y(\mathbf{v}) = \lambda^r \int_{Y_2} \rho^2 \boldsymbol{\varphi}^r \cdot \mathbf{v} \quad \forall \mathbf{v} \in \mathbf{H}_0^1(Y_2), \quad \int_{Y_2} \rho^2 \boldsymbol{\varphi}^r \cdot \boldsymbol{\varphi}^s = \delta_{rs}. \quad (4)$$

To simplify the notation, the *eigenmomentum*  $\mathbf{m}^r = (m_i^r)$ , and the averaged density  $\langle \rho \rangle$  are introduced:

$$\mathbf{m}^r = \int_{Y_2} \rho^2 \boldsymbol{\varphi}^r, \quad \langle \rho \rangle = \sum_{k=1,2} \int_{Y_k} \rho^k. \quad (5)$$

Due to the above definition of  $\mathbf{m}^r$ , in what follows we confine spectrum with the following index set:

$$\mathcal{R} = \{r \in \mathbb{N} \mid (\lambda^r, \boldsymbol{\varphi}^r) \text{ solve (4)}, \mid \int_{Y_2} \rho^2 \boldsymbol{\varphi}^r \mid > 0\}. \quad (6)$$

The macroscopic model of the acoustic wave propagation in the homogenized medium is introduced in terms of the following tensors, all depending on  $\omega^2$ :

---

<sup>3</sup>Often called the effective material parameters.

- *Mass tensor*  $\mathbf{M} = (M_{ij})$

$$M_{ij}(\omega^2) = \frac{1}{|Y|} \int_Y \rho \delta_{ij} - \frac{1}{|Y|} \sum_{r \in \mathcal{R}} \frac{\omega^2}{\omega^2 - \lambda^r} m_i^r m_j^r ; \quad (7)$$

- *Applied load tensor*  $\mathbf{B} = (B_{ij})$

$$B_{ij}(\omega^2) = \delta_{ij} - \frac{1}{|Y|} \sum_{r \in \mathcal{R}} \frac{\omega^2}{\omega^2 - \lambda^r} m_i^r \int_{Y_2} \varphi_j^r .$$

The *elasticity coefficients*  $\mathbb{D} = (D_{ijkl})$  are computed using the same formula as the one obtained for the homogenized perforated domain, thus being independent of the material in inclusions:

$$D_{ijkl} = \frac{1}{|Y|} \int_{Y_1} [\mathbb{C}^1 \mathbf{e}^y(\mathbf{w}^{kl} + \mathbf{\Pi}^{kl})] : \mathbf{e}^y(\mathbf{w}^{ij} + \mathbf{\Pi}^{ij}) , \quad (8a)$$

where  $\mathbf{\Pi}^{kl} = (\Pi_i^{kl}) = (y_l \delta_{ik})$  and  $\mathbf{w}^{kl} \in \mathbf{H}_{\#}^1(Y_1)$  are the corrector functions satisfying

$$\int_{Y_1} [\mathbb{C}^1 \mathbf{e}^y(\mathbf{w}^{kl} + \mathbf{\Pi}^{kl})] : \mathbf{e}^y(\mathbf{v}) = 0 \quad \forall \mathbf{v} \in \mathbf{H}_{\#}^1(Y_1) . \quad (8b)$$

Above  $\mathbf{H}_{\#}^1(Y_1)$  is the restriction of  $\mathbf{H}^1(Y_1)$  to the  $Y$ -periodic functions (periodicity w.r.t. the homologous points on the opposite edges of  $\partial Y$ ).

The *global equation* — the macromodel — involves the homogenized coefficients. We find  $\mathbf{u} \in \mathbf{H}_0^1(\Omega)$  such that

$$-\omega^2 \int_{\Omega} [\mathbf{M}(\omega^2) \mathbf{u}] \cdot \mathbf{v} + \int_{\Omega} [\mathbb{D} \mathbf{e}(\mathbf{u})] : \mathbf{e}(\mathbf{v}) = \int_{\Omega} [\mathbf{B}(\omega^2) \mathbf{f}] \cdot \mathbf{v} \quad \forall \mathbf{v} \in \mathbf{H}_0^1(\Omega) . \quad (9)$$

## 2.4 Band gap prediction

Heterogeneous periodic structures with finite scale of heterogeneities exhibit the frequency *band gaps* — for certain frequency bands the wave propagation is disabled, or restricted in the polarization, cf. [42]. In the *homogenized medium*, the wave propagation depends on the positivity of mass tensor  $\mathbf{M}(\omega)$ . Thus, as the main advantage of the homogenized model derived in [4], by analyzing the dependence  $\omega \mapsto \mathbf{M}(\omega)$ , one can determine bounds of the band gaps with significantly less effort than in case of computing them in the standard way, see e.g. [41].

The band gaps can be classified w.r.t. the polarization of waves which cannot propagate. We now summarize the results of [4] and [38]. There are three principal modes of the wave propagation which are distinguished below according to the signs of eigenvalues  $\gamma^r(\omega)$ ,  $r = 1, \dots, d$  of the mass tensor  $\mathbf{M}(\omega)$  analyzed for a given frequency  $\omega$ ; more precisely, we consider

$$\gamma^r : \mathbb{R}^+ \setminus \{\lambda^k\}_{k \in \mathbb{N}} \rightarrow \mathbb{R} \text{ such that } (\mathbf{M}(\omega) - \gamma^r(\omega) \mathbf{I}) \mathbf{v}^r = \mathbf{0} , \quad |\mathbf{v}^r| = 1 . \quad (10)$$

Further we consider the ordering  $\gamma^1(\omega) \leq \gamma^2(\omega) \leq \dots \leq \gamma^d(\omega)$  for any “nonresonant”  $\omega \neq \sqrt{\lambda^k}$ ,  $k = 1, 2, \dots$ . In general,  $\gamma^1 \rightarrow -\infty$  for  $\omega \searrow \sqrt{\lambda^k}$  and  $\gamma^d \rightarrow \infty$  for  $\omega \nearrow \sqrt{\lambda^{k+1}}$ , see Figure 1.

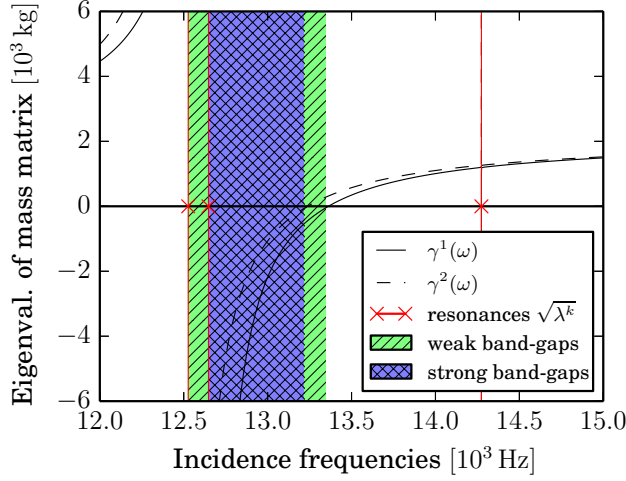


Figure 1: The distribution of band gaps, resonances, and eigenvalues of mass matrix for a periodic cell with an oval inclusion which is obtained as a perturbation of the circular inclusion; all types of frequency bands (weak band gap, strong band gap, and propagation zone) can be observed.

Let us denote by  $\omega_k^r$  the root of the eigenvalue  $\gamma^r(\omega)$  within a particular interval between adjacent eigenvalues of problem (4), thus

$$\omega_k^r \in ]\sqrt{\lambda^k}, \sqrt{\lambda^{k+1}}[ \text{ such that } \gamma^r(\omega_k^r) = 0. \quad (11)$$

Such a root may not exist for any  $\gamma^r(\omega)$ , however.

In Section 4, when dealing with the band gap optimization problem, we assume that the root  $\omega_k^1$  exists<sup>4</sup>, see Remark 2(v). Under this assumption, the wave propagation for  $\omega$  in the interval  $] \sqrt{\lambda^k}, \omega_k^1[$  is restricted to the waves with the local polarizations  $\mathbf{u}(x)$  orthogonal to eigenvector  $\mathbf{v}^1$  and also to all other  $\mathbf{v}^s$ ,  $s \in \{2, \dots, d\}$  for which  $\gamma^s(\omega) < 0$ . For more details we refer to [38] and [42], where this topic was discussed in detail. Depending on the frequency considered,  $\omega \in ] \sqrt{\lambda^k}, \omega_k^1[$  and on the existence of other roots  $\omega_k^r$ ,  $r \in \{2, \dots, d\}$ , the following 3 cases of the wave propagation can be distinguished:

1. Non-restricted propagation:  $d$  waves governed by the homogenized model (9) can propagate without any restriction of the wave polarization; this can only happen for  $\omega \in P_k := ] \omega_k^1, \sqrt{\lambda^{k+1}}[$ .
2. No wave can propagate, if all eigenvalues of  $\gamma^r(\omega)$ ,  $r = 1, \dots, d$  are negative, so that the mass tensor  $\mathbf{M}(\omega)$  is negative definite. This only can happen, if the root  $\omega_k^d$  exists, for frequencies  $\omega \in G_k^S := ] \sqrt{\lambda^k}, \omega_k^d[$ .
3. Propagation is possible only for waves polarized in a manifold determined by eigenvectors  $\mathbf{v}^r$  associated with positive eigenvalues  $\gamma^r(\omega) > 0$ . Tensor  $\mathbf{M}(\omega)$  is indefinite for a such given  $\omega$ , i.e. there is at least one negative and one positive eigenvalue,  $\gamma^1(\omega) < 0 < \gamma^d(\omega)$ .

In general, any interval  $\Lambda_k := ] \sqrt{\lambda^k}, \sqrt{\lambda^{k+1}}[$  splits into three bands characterized by the above three cases and the three corresponding sets  $P_k$  and  $G_k^S$ , and  $G_k^W$ , whereby  $G_k^W := \Lambda_k \setminus (G_k^S \cup P_k)$ ,

<sup>4</sup>Note that  $\omega_k^r \leq \omega_k^{r-1}$  for any two existing roots.



1. **strong band gap**  $G_k^S := \{\omega \in \Lambda_k | \gamma^s(\omega) < 0, \forall s = 1, \dots, d\}$ .
2. **weak band gap**  $G_k^W := \{\omega \in \Lambda_k | \gamma^1(\omega) < 0 \text{ and } \gamma^d(\omega) > 0\}$ .
3. **propagation zone**  $P_k := \{\omega \in \Lambda_k | \gamma^s(\omega) > 0, \forall s = 1, \dots, d\}$ .

For illustration, in Figure 1, the three sets are depicted and the curves  $\gamma^r(\omega)$  are displayed. We conclude this section by following comments:

**Remark 2.**

- (i) The above definition of the weak band gap  $G_k^W$  is not explicit in the sense that it depends on the existence of  $P_k$  and  $G_k^S$ . However, none of these can be guaranteed.
- (ii) Functions  $\gamma^r(\omega)$  are monotone in  $\Lambda_k$ .
- (iii) It may happen that  $\gamma^1(\omega) < 0$  for all  $\omega \in \Lambda_k$ , which would mean that  $P_k = \emptyset$ .
- (iv) If inclusions (considered in 2D) are symmetric w.r.t. more than 1 axis of symmetry, then only strong band gaps exist; the band gap properties and their relationship to the dispersion of guided waves were discussed in [38].
- (v) In what follows we shall consider only such situations where  $P_k \neq \emptyset$  and  $G_k^W \neq \emptyset$ . Therefore, we assume existence of the root  $\omega_k^1 \in \Lambda_k$ , so that  $G_k^W = ]\sqrt{\lambda^k}, \omega_k^1[$ . Note that, if such a  $\omega_k^1$  does not exist within  $\Lambda_k$  for a particular  $k$ , the weak band gap spans over the whole interval  $\Lambda_k$ , hence  $P_k = \emptyset$ . For example, this situation arises when a symmetric shape  $Y_2$  with two axes of symmetry is slightly perturbed, so that a resonance value  $\lambda^k$  with multiplicity 2 splits into two closed values  $\lambda^k$  and  $\lambda^{k+1}$ , as reported in Figure 1.

△

### 3 Rescaling and interpretation of the results

As pointed out above, see Remark 1, for interpretation of the limit model, it is necessary to consider a given “fixed scale”  $\varepsilon = \varepsilon_0$ , which yields the elasticity tensor  $\bar{\mathbf{C}}^2 := \mathbf{C}^{\text{phys}}/\varepsilon_0^2$ . In this section we discuss how the band gap distribution depends on the real microstructure size of the heterogeneity and on the material contrast, cf. [38].

For elasticity tensor  $\mathbf{C}^{2,\varepsilon} = \mathbf{C}^{\text{phys}}$  of a given existing material and for a given microstructure represented by the inclusion  $Y_2$  placed in the unit periodic cell  $Y$ , simple rescaling of the eigenvalue problem (4) yields the following equivalent problem imposed in the “real-sized” inclusion  $\varepsilon Y_2$ ,

$$\int_{\varepsilon Y_2} \mathbf{C}^{2,\varepsilon} e^x(\varphi^\varepsilon) : e^x(v) = \lambda^\varepsilon \int_{\varepsilon Y_2} \rho^2 \varphi^\varepsilon \cdot v \quad \forall v \in \mathbf{H}_0^1(Y_2), \quad \int_{Y_2} \rho^2 \varphi^r \cdot \varphi^s = \delta_{rs}. \quad (12)$$

whereby, the eigenvalues  $\lambda^\varepsilon$  are equivalent to the ones computed in (4), *i.e.*  $\lambda = \lambda^\varepsilon$  and also  $\varphi = \varphi^\varepsilon$ .

As the consequence, for describing the band gaps by analyzing homogenized mass tensor  $\mathbf{M}(\omega)$ , the eigenvalue problem has to be solved either in the reference domain  $Y_2$  with the rescaled coefficients  $\bar{\mathbf{C}}^2$ , or equivalently using (12) with “true” coefficients  $\mathbf{C}^{\text{phys}}$  (in the sense of Remark 1) and the real-sized inclusion  $\varepsilon Y_2$ .

problem	$\varepsilon$	$\bar{E}_2$ [Pa]	$\sqrt{\lambda^2}$	$\omega_2^1$	$\sqrt{\lambda^3}$	BG type
circle	1	$3.772 \cdot 10^9$	$1.2511 \cdot 10^4$	$1.3182 \cdot 10^4$	$1.4005 \cdot 10^4$	strong
	0.1	$3.772 \cdot 10^7$	$1.2511 \cdot 10^5$	$1.3182 \cdot 10^5$	$1.4005 \cdot 10^5$	
	0.01	$3.772 \cdot 10^5$	$1.2511 \cdot 10^6$	$1.3182 \cdot 10^6$	$1.4005 \cdot 10^6$	
diamond	1	$3.772 \cdot 10^9$	$1.3234 \cdot 10^4$	$1.3898 \cdot 10^4$	$1.5564 \cdot 10^4$	strong
	0.1	$3.772 \cdot 10^7$	$1.3234 \cdot 10^5$	$1.3898 \cdot 10^5$	$1.5564 \cdot 10^5$	
	0.01	$3.772 \cdot 10^5$	$1.3234 \cdot 10^6$	$1.3898 \cdot 10^6$	$1.5564 \cdot 10^6$	
L-shape	1	$3.772 \cdot 10^9$	$1.6596 \cdot 10^4$	$1.7167 \cdot 10^4$	$2.0934 \cdot 10^4$	weak
	0.1	$3.772 \cdot 10^7$	$1.6596 \cdot 10^5$	$1.7167 \cdot 10^5$	$2.0934 \cdot 10^5$	
	0.01	$3.772 \cdot 10^5$	$1.6596 \cdot 10^6$	$1.7167 \cdot 10^6$	$2.0934 \cdot 10^6$	

Table 1: Illustration of the spectral properties and the 2nd weak band gap dependence on the microstructure size. The material is the aluminium-epoxy composite. The Young's modulus and the Poisson's ratios for the epoxy resin inclusion are  $E_2 = 3.772$  GPa and  $\nu_2 = 0.2743$ , respectively; densities  $\rho_1$  and  $\rho_2$  are introduced in Table 3. The frequencies  $(\sqrt{\lambda^1}, \sqrt{\lambda^2}, \omega_2^1)$  are in [Hz]. The rescaled modulus is given by  $\bar{E}_2 = \varepsilon^{-2} E_2$ .

**Remark 3.** (*Two-phase piecewise constant material.*) When dealing with an optimal material design problem, it is quite natural to consider a composite material formed by two homogeneous components. Therefore, in what follows, with reference to the definition (2), we shall consider  $\mathbb{C}^1$ ,  $\bar{\mathbb{C}}^2$  and  $\rho^\beta$ ,  $\beta = 1, 2$  as constants independent of the position  $y \in Y$ . With this assumption in hand much of the subsequent development could be simplified.

△

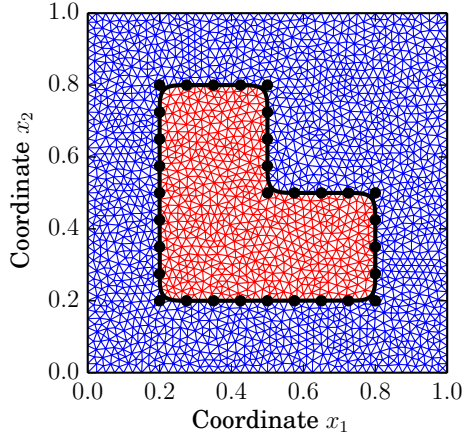
### 3.1 Influence of the size of the microstructure

As explained above, the spectrum given equivalently by (4), or (12), depends on  $\varepsilon$ . In this paragraph we explore how the band gap distribution changes with the characteristic size of the microstructure, whereby the material properties of the composite are fixed.

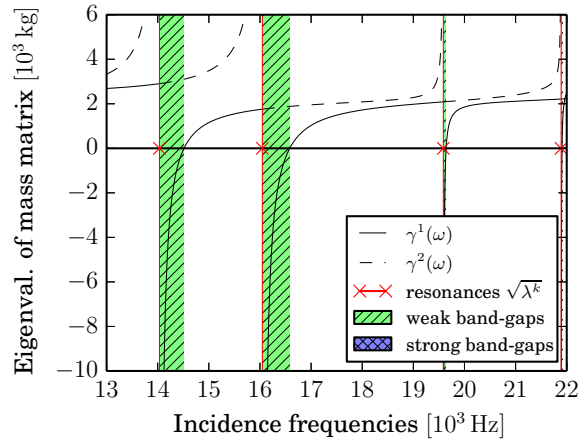
To illustrate the size effect, we may consider two structures characterized by  $\varepsilon_0$  and  $\varepsilon_1$ , respectively, but both composed of the same two materials, the aluminium situated in  $Y_1$ , and epoxy resin situated in  $Y_2$ , with a given fixed volume fraction. The transformation formulas are derived in A. In Tab. 1, for different  $a = \varepsilon_1/\varepsilon_0$  and different shapes of inclusion  $Y_2$  depicted in Fig. 3, the spectral responses of three the phononic structures are compared in terms of the two resonant frequencies,  $\sqrt{\lambda^2}, \sqrt{\lambda^3}$  and the second band gap bounds, such that  $G_2^W = ]\sqrt{\lambda^2}, \omega_2^1]$ . As the rule of the scaling, by getting the structure smaller with the factor  $a < 1$ , any frequency band is multiplied by factor  $1/a$ ; as the consequence, the band gaps become wider, being shifted to higher frequency ranges.

We depict the size effect in Figures 2 (ab) and (cd), where the band gap distribution, eigenvalues of mass matrix, and resonance frequencies are plotted for two sizes of periodic cell,  $\varepsilon = 1$  and  $\varepsilon = 0.5$ , respectively.

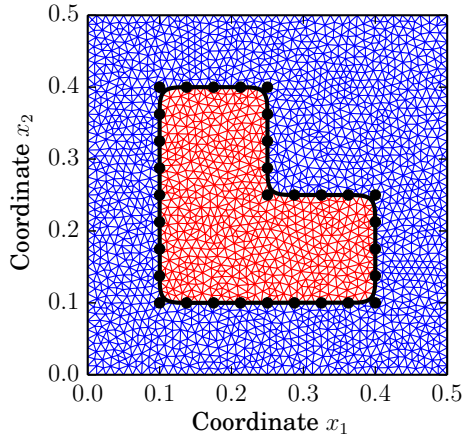
It can be seen that decreasing the microstructure size by 1/2 produces an increase of the frequencies  $\{\sqrt{\lambda^r}\}$ ,  $r \in \mathcal{R}$  of the spectrum by the corresponding factor of 2; thus, all the relevant properties are invariant under rescaling the frequency axis, see the difference between Figures 2 (b) and (d).



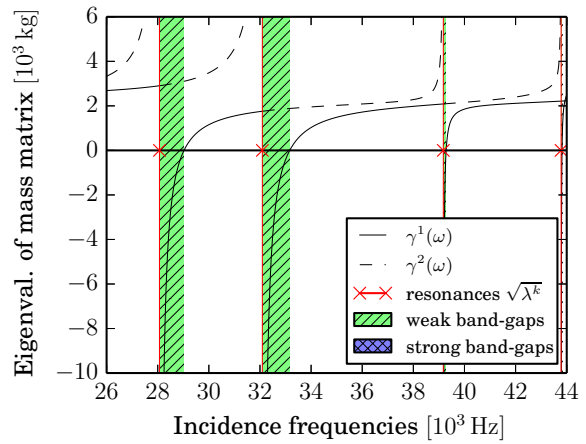
(a) Mesh with inclusion



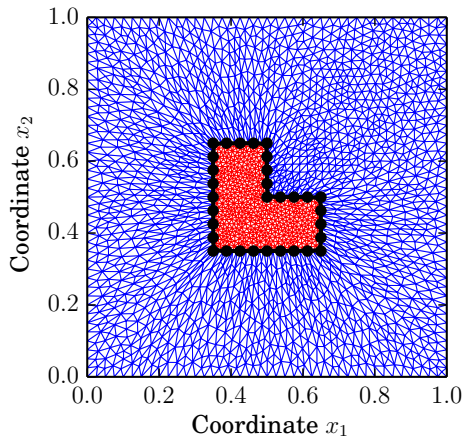
(b) band gaps and resonance frequencies



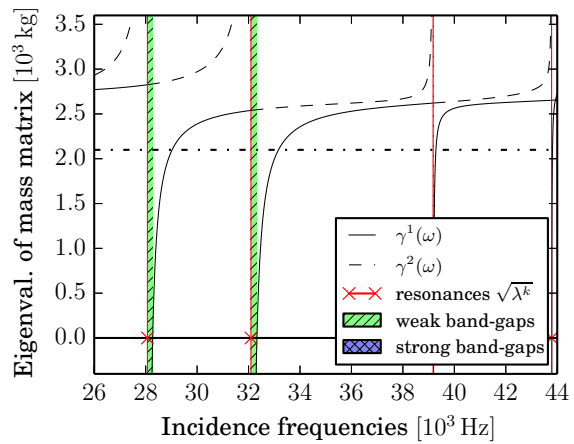
(c) Mesh with inclusion



(d) band gaps and resonance frequencies



(e) Mesh with inclusion



(f) band gaps and resonance frequencies

Figure 2: The distribution of band gaps, resonances, and eigenvalues of mass matrix for different sizes of periodic cell and L-shaped inclusion; in (f), the dot-and-dash line represent the initial  $x$ -axis in (b) and (d), which is shifted by  $\rho_1(1 - \kappa^d)/\kappa^d = 2.099 \cdot 10^3 \text{ Hz}$  for  $d = 2$  and  $\kappa = 2$ .

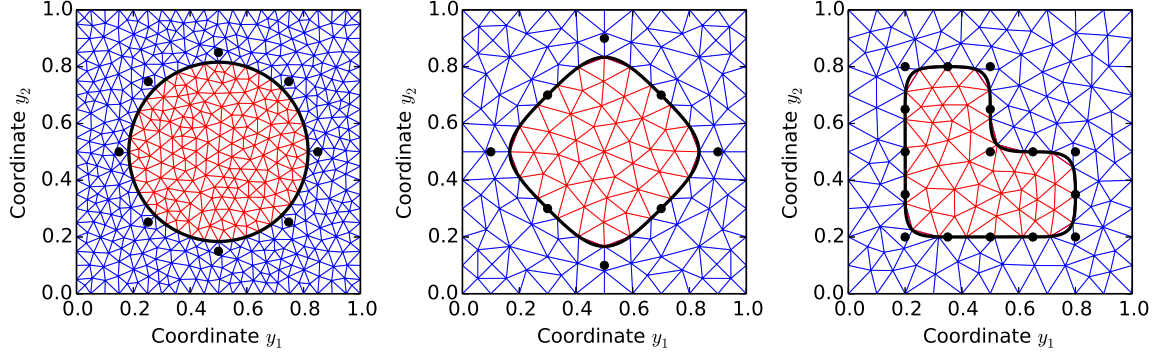


Figure 3: Shapes of inclusions used in Tab. 1 (left to right): circle, diamond, L-shape.

### 3.2 Effect of volume fraction $|Y_2|/|Y|$

Intuitively, by increasing the volume fraction  $\phi_2 = |Y_2|/|Y|$ , phononic structures with large band gaps can be designed while retaining the range of frequencies. In the previous section, we have discussed the proportional scaling of the whole microstructure, which produces the corresponding scaling of frequencies. In Figure 4 and Table 2, we show more complicated change of the volume fraction  $|Y_2|/|Y|$  between inclusion and periodic cell. As illustrated in Figures 2 (ab) and (ef), the change of the inclusion size leads to a combined effect as both horizontal axis of frequencies is linearly scaled while the vertical axis of mass matrix eigenvalues is mapped by affine transformation.

To explain this phenomenon, let us consider the following affine mapping  $\mathcal{F}_\kappa : y_i \mapsto \kappa(y_i - \bar{y}_i) + \bar{y}_i$ ,  $i = 1, \dots, d$ , where  $(\bar{y}_i) = \bar{y} \in Y$  is a given point and  $\kappa \in \mathbb{R}^+$ . We introduce new coordinates  $z_i = \kappa(y_i - \bar{y}_i) + \bar{y}_i$  for  $y \in Y_2$ . This transforms the inclusion  $Y_2$  to  $Z_2 = \mathcal{F}_\kappa(Y_2)$ , whereby  $\bar{Z} \subset Y$  and  $Z_1 := Y \setminus \bar{Z}$  is the transformed matrix part; obviously, there exists a homeomorphic mapping  $\mathcal{G}_\kappa : y \mapsto z$ , such that  $Z_1 := \mathcal{G}_\kappa(Y_1)$ , however, we do not need to know this mapping as far as the material in  $Y_1$  is homogeneous. Thus, the decomposition of the periodic unit cell transforms to  $Y = Z_1 \cup \bar{Z}$ . By  $\tilde{A}$  we denote the corresponding quantity  $A$  defined in sub-cells  $Z_1$  and  $Z_2$  obtained by transformations  $\mathcal{G}_\kappa$  and  $\mathcal{F}_\kappa$ . We shall now derive the transformed averaged density  $\langle \tilde{\rho} \rangle$ . Noting that  $\det(\nabla_y \mathcal{F}_\kappa) = \kappa^d$ , thus  $|Z_2| = \kappa^d |Y_2|$ , we derive

$$\begin{aligned} \langle \tilde{\rho} \rangle &= \sum_{\beta=1,2} \rho^\beta \frac{|Z_\beta|}{|Y|} = \frac{\kappa^d}{|Y|} \sum_{\beta=1,2} \rho^\beta + \frac{\rho^1}{|Y|} (1 - \kappa^d |Y_2|) - \rho^1 \kappa^d |Y_1| \\ &= \kappa^d \langle \rho \rangle + \rho^1 (1 - \kappa^d), \end{aligned}$$

where  $\langle \rho \rangle$  is given by (5)<sub>2</sub>. The transformed eigenvalue problem yields spectral elements  $(\tilde{\lambda}^r, \tilde{\varphi}^r)$  satisfying (4) transformed by  $\mathcal{F}_\kappa$  (note  $\nabla_z = \kappa^{-1} \nabla_y$ )

$$\begin{aligned} \int_{Z_2} [\bar{\mathbf{C}}^2 e^z(\tilde{\varphi}^r)] : e^z(v) &= \tilde{\lambda}^r \int_{Y_2} \rho^2 \tilde{\varphi}^r \cdot v, \quad \int_{Z_2} \rho^2 \tilde{\varphi}^r \cdot \tilde{\varphi}^s = \delta_{rs}, \\ \Leftrightarrow \\ \int_{Y_2} \kappa^{-2} [\mathbf{C}^2 e^y(\tilde{\varphi}^r(z(y)))] : e^y(\tilde{v}) \kappa^d &= \tilde{\lambda}^r \int_{Y_2} \rho^2 \tilde{\varphi}^r(z(y)) \cdot \tilde{v} \kappa^d, \quad \int_{Y_2} \rho^2 \tilde{\varphi}^r(z(y)) \cdot \tilde{\varphi}^s(z(y)) \kappa^d = \delta_{rs}, \end{aligned}$$

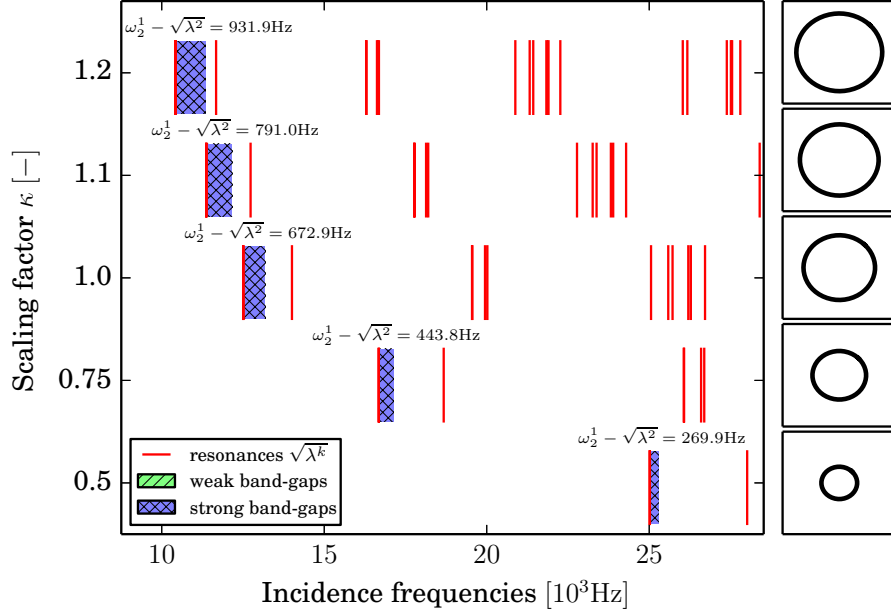


Figure 4: The change of band-gap size depending on a change of inclusion size by the scaling factor  $\kappa$ .

for all  $\mathbf{v} \in \mathbf{H}_0^1(Z_2)$  and all  $\tilde{\mathbf{v}} \in \mathbf{H}_0^1(Y_2)$ , which reveals

$$\begin{aligned}\tilde{\lambda}^s &= \kappa^{-2}\lambda^s, \quad \tilde{\varphi}^s(z(y)) = \kappa^{-d/2}\varphi^s(y), \quad s \in \mathcal{R}_\theta, \\ \widetilde{\mathbf{m}}^s &:= \int_{Z_2} \rho^2 \tilde{\varphi}^s = \int_{Y_2} \rho^2 \kappa^{-d/2} \varphi^s(y) \kappa^d = \kappa^{d/2} \varphi^s.\end{aligned}$$

Hence, by invoking the definition (7) of  $\mathbf{M}(\omega)$  transformed by  $\mathcal{F}_\kappa$  and using the observation listed in Section 3.2, we can derive the following expression:

$$\begin{aligned}\widetilde{\mathbf{M}}(\omega) &= \langle \widetilde{\rho} \rangle \mathbf{I} - \frac{1}{|Y|} \sum_{r \in \mathcal{R}_\theta} \frac{\omega^2}{\omega^2 - \tilde{\lambda}^r} \widetilde{\mathbf{m}}^r \otimes \widetilde{\mathbf{m}}^r \\ &= \left( \kappa^d \langle \rho \rangle + \rho^1 (1 - \kappa^d) \right) \mathbf{I} - \frac{1}{|Y|} \sum_{r \in \mathcal{R}_\theta} \frac{\kappa^2 \omega^2}{\kappa^2 \omega^2 - \lambda^r} \kappa^{d/2} \mathbf{m}^r \otimes \kappa^{d/2} \mathbf{m}^r \\ &= \kappa^d \mathbf{M}(\kappa \omega) + \rho^1 (1 - \kappa^d) \mathbf{I}.\end{aligned}\tag{13}$$

It is worth to note that for  $\kappa > 1$ , the frequency bands relevant to  $\widetilde{\mathbf{M}}$  are decreased as well as the eigenvalues due to the negative second term in (13). This provokes an extension of the band gaps, see the discussion below and Figure 4 which illustrates this effect for the circular inclusion and the variation  $\kappa \in \{0.5, 0.75, 1.0, 1.1, 1.2\}$ .

### 3.3 Discussion of the rescaling and resizing effects

It has been shown in Section 3.1, how the structure size modifies the range of frequencies. In this paragraph and in A, we denote by  $\underline{\omega}$  and  $\bar{\omega}$  the lower and upper band gap bounds, respectively; the same notation is adhered in Tab. 2. In particular, the band gap  $G^{\varepsilon_0}$  of periodic structures

$\kappa$	$\sqrt{\lambda_2}$	$\bar{\omega}$	$\sqrt{\lambda_3}$	$\bar{\omega} - \underline{\omega}$
0.5	$2.5021 \cdot 10^4$	$2.5289 \cdot 10^4$	$2.8011 \cdot 10^4$	268.1
0.75	$1.6680 \cdot 10^4$	$1.7123 \cdot 10^4$	$1.8674 \cdot 10^4$	442.6
1.0	$1.2510 \cdot 10^4$	$1.3182 \cdot 10^4$	$1.4005 \cdot 10^4$	672.1
1.1	$1.1373 \cdot 10^4$	$1.2163 \cdot 10^4$	$1.2732 \cdot 10^4$	790.2
1.2	$1.0425 \cdot 10^4$	$1.1357 \cdot 10^4$	$1.1671 \cdot 10^4$	931.2

Table 2: Effect of volume fraction. Notation:  $\underline{\omega} = \sqrt{\lambda_2}$  is the lower bound,  $\bar{\omega} = \omega_2^1$  is the upper bound of the 2nd weak band gap.

characterized by the scale  $\varepsilon_0 \ll 1$  can be obtained easily by rescaling the band gap  $G^1 = ]\underline{\omega}, \bar{\omega}[$  computed for fictitious scale  $\varepsilon = 1$  by factor  $1/\varepsilon^0$ , so that  $G^\varepsilon = 1/\varepsilon^0 ]\underline{\omega}, \bar{\omega}[$ . This simple rule reveals limitations of exploiting the band gap effect in an audible frequency range (up to 20 kHz) for a given contrast of the two materials. On one hand, for the structure with  $\varepsilon = 0.01$ , such that the real-sized cell  $\varepsilon Y$  is the square  $1 \times 1$  cm, the first band gap is in the range of 1000 kHz, see Table 1. On the other hand, for larger structures, say  $\varepsilon \approx 1$  for which the band gaps are predicted in the range of 10 kHz, the model is not relevant, since the characteristic size of the heterogeneities is comparable with wave lengths<sup>5</sup>.

To allow for small structures with the characteristic size  $\approx 1$  cm and the band gaps in the audible spectrum, much softer material would need to be used to keep the resonant frequencies in the inclusion under the 1 kHz. This can be achieved by means of resonators occupying  $Y_2$  which themselves are inhomogeneous, being designed as a coated heavy particles; as an example, a hard sphere (in  $\mathbb{R}^d$ ) forming the central part coated by a very compliant, though light material, can serve the desired property of a low stiffness due to the coating and a large mass due to the central part.

The second study reported in Section 3.2 demonstrates the quite natural effect of shifting the band gaps to lower frequency bands. As another effect of such design modification, the eigenvalues  $\tilde{\gamma}(\omega)$  of tensor  $\widetilde{\mathbf{M}}(\omega)$  become smaller (in comparison with  $\gamma(\kappa\omega)$ ) which leads to an extension of the band gaps due to the increased roots  $\tilde{\omega}^s$ ,  $s = 1, \dots, d$  for which  $\tilde{\gamma}^s(\tilde{\omega}^s) = 0$ .

For completeness, we remark that  $|Y_2|/|Y|$  can also be achieved by keeping the inclusion volume  $|Y_2|$  unchanged while changing the cell size (note that  $|Y| \neq 1$ ). In this case depicted by Figures 2 (cd) and (ef), the change of the cell size keeps the resonance frequencies because they depend on the same inclusion shape and size. The eigenvalues of mass matrix are scaled with affine transformation, however their qualitative behavior remains the same as the shapes of corresponding curves are identical in (d) and (f); in (f), the dash-and-dot line depict the initial horizontal axis from (b) or (d). Therefore, the size of band gaps heavily depends on volume fraction; importantly, its size can be easily predicted a posteriori, without recalculation of eigenvalues problem (12).

The following remark is devoted to the *choice of the unit cell*  $Y$ .

**Remark 4.** The unit cell  $Y = ]0, 1[^d$  is the simplest and the most often used cell to generate a periodic structure, although  $Y$  can be chosen more generally as a parallelepiped. The assumption  $|Y| = 1$  is frequently used, but not mandatory. In classical homogenization, in the effective properties do not depend on the size of  $Y$ , although the scale separation in the context of  $\varepsilon$  being small is understood in the sense  $|Y| = O(1)$ . In our situation, the effective mass  $\mathbf{M}(\omega)$  depends on the size of the microstructure, *i.e.* on the scale, as discussed in Section 3.1, and on the volume fraction

<sup>5</sup>For the composite made of the aluminium alloy matrix and the epoxy inclusions, the wave lengths of waves at  $\omega = 14$  kHz are at the range of  $\approx 1$  m; with reference to Tab. 1, for  $\varepsilon \in \{1, 0.1, 0.01\}$ , the respective wavelengths are  $\{2.89, 2.01, 1.52\}$  m.

$\phi_2 = |Y_2|/|Y| = 1 - \phi_1$ , as discussed in Section 3.2. Contrary to this observation, the elasticity  $\mathbb{D}$  defined in (8a) does not depend on the scale of the structure, however, it depends on the mutual relationship between the shapes of the inclusion,  $Y_2$ , and their relative positions. Indeed, while keeping the shape of  $Y_2$  and the fraction  $\phi_1$  constant, *i.e.*  $|Y| = 1$ , different effective elasticity of the homogenized medium is computed when changing the ratios of the 2 diagonals in the parallelepiped  $Y$ . By virtue of the periodicity, such arrangement with nonorthogonal faces of  $Y$  corresponds to different relative placements of inclusions in the composite.

△

## 4 Optimal design of the phononic structures

We focus on the problem of maximization of one of the lowest band gaps by means of changing the shape of inclusions  $Y_2$ . Due to the scaling properties presented in Section 3.1, the optimization can be related to the unit cell  $Y$ . The required frequencies of band gaps can be obtained a posteriori by choosing the appropriate microstructure size, *i.e.* scaling the unit cell by an appropriate factor, see A, to obtain a required frequency range.

We assume the composite is made of two materials in the sense of Remark 3. For a given  $k \geq 1$ , the objective function can be defined in terms of the band gaps  $G_k^S$  or  $G_k^W$ :

$$\Phi_S = |G_k^S|, \quad \Phi_W = |G_k^S| + |G_k^W|.$$

Since the existence of  $G_k^S$  is guaranteed for symmetric shapes of  $Y_2$  only, cf. [4], whereas  $|G_k^W| > 0$  whenever  $\lambda^{k+1} > \lambda^k$ , we chose rather the function  $\Phi_W$  to express the optimality criterion. By virtue of the Remark 2(v) we shall assume the existence of  $\omega_k^1$  such that  $\gamma^1(\omega_k^1) = 0$  and define the objective function

$$\Phi_k = \omega_k^1 - \sqrt{\lambda^k}. \quad (14)$$

From now on we shall rather restrict to 2D problems, thus, we consider  $d = 2$ . The optimization problem is presented in three steps: First we introduce the shape parameterization of domain  $Y_2$ , then we summarize the constraints which make the link between the design parameters and the state variables, finally we formulate the optimization problem.

### 4.1 Shape parameterization

We are interested in variation of the shape of the inclusion  $Y_2$  bounded by the interface  $\Gamma_{12} = \partial Y_2$ . We assume existence of a design parameterization, such that

$$\begin{aligned} Y_2 &\text{ is nonempty, simply connected Lipschitz domain;} \\ \Gamma_{12} &\subset Y, \text{ thus, } \text{dist}(\Gamma_{12}, \partial Y) > 0. \end{aligned} \quad (15)$$

The shape of  $Y_2$  can be defined by a smooth curve described by a finite number of design variables  $\alpha$ . For this, we introduce a smooth mapping  $\Sigma : \alpha \mapsto \Gamma_{12}(\alpha)$ . In our work,  $\Sigma$  is defined in terms of the cyclic spline parametrization of the closed curve  $\Gamma_{12}$ . By  $\{\mathbf{P}^i\}_{i=0}^{n-1}$ , where  $\mathbf{P}^i = (P_j^i)$  we denote the control polygon of a B-spline of order  $p < n$ , where  $n$  is the number of the control points  $\mathbf{P}^i \in \mathbb{R}^2$ . We consider the uniform parametrization defined by the knot vector  $\mathbf{t} = \{t_i\}$  with  $t_i = i$  for  $i \in \mathbb{Z}$ , such that any point  $y(t) \in \Gamma_{12}$  is expressed by

$$y_j(t) = \sum_{i=0}^{n-1} P_j^i \bar{B}_{i,p}(t), \quad (16)$$

where  $\bar{B}_{i,p}(t)$  are the B-spline basis functions.

The control points  $\mathbf{P}^i$  are modified by the design variables  $\boldsymbol{\alpha}^i$ . In particular, the modified interface  $\Gamma_{12}(\boldsymbol{\alpha})$  is given according to (16) where  $\mathbf{P}^i := \mathbf{X}^i + \boldsymbol{\alpha}^i$  with the “initial shape”,  $\Gamma_{12}^0 = \Gamma_{12}(\mathbf{0})$  defined by the polygon  $\{\mathbf{X}^i\}$ , so that

$$\Gamma_{12}(\boldsymbol{\alpha}) = \left\{ y_j(t) = \sum_{i=0}^{n-1} (X_j^i + \alpha_j^i) \bar{B}_{i,p}(t), \quad j = 1, 2 \quad \text{for any } t \in [0, n] \right\}.$$

Admissible designs of the inclusion  $Y_2$  are generated by  $\boldsymbol{\alpha}^i \in \mathcal{A} = \{\boldsymbol{\alpha} \in \mathbb{R}^{2 \times (n-1)} : (15) \text{ hold}\}$ .

By virtue of Remark 3, *i.e.* assuming two constant materials distributed in  $Y_1$  and  $Y_2$ , respectively, the objective function depends only on the shape of  $\Gamma_{12}$ . However, to derive the sensitivity analysis formulas and to handle the numerical model associated with a computational finite element partitioning, we need to introduce a parametrization of domain  $Y$ . Let  $Y_\beta(\boldsymbol{\alpha})$ ,  $\beta = 1, 2$  be the domains shaped by  $\Gamma_{12}(\boldsymbol{\alpha})$ , recalling  $\partial Y$  is fixed. Further let  $Y_\beta^0$  be the reference (initial) domains<sup>6</sup>; obviously  $Y_1^0 \cup Y_2^0 \cup \Gamma_{12}^0 = Y$ . For a modified design represented by  $\boldsymbol{\alpha}$  we introduce a smooth mapping  $\mathcal{F} : (\boldsymbol{\alpha}, Y_\beta^0) \mapsto Y_\beta(\boldsymbol{\alpha})$  such that

$$\begin{aligned} Y_\beta(\boldsymbol{\alpha}) &= \{y + \vec{\mathcal{U}}(y, \boldsymbol{\alpha}), \text{ where } y \in Y_\beta^0\}, \\ \vec{\mathcal{U}}(y, \boldsymbol{\alpha}) &= \sum_{i=0}^{n-1} \sum_{j=1}^2 \alpha_j^i \vec{\mathcal{V}}^{i(j)}(y), \quad y \in Y_\beta^0, \end{aligned} \quad (17)$$

where  $\mathcal{V}_k^{i(j)}$ ,  $k = 1, 2$  are components of the so-called “design velocity field” associated with the optimization variable  $\alpha_j^i$ . There are various approaches how to establish  $\vec{\mathcal{V}}^{i(j)}$ . A simple one is based on the following auxiliary elasticity problems imposed in  $Y_1^0 \cup Y_2^0$ : for  $i \in \{0, 1, \dots, n-1\}$ , being associated with the control points  $\mathbf{P}^i$  of the B-spline, and  $j \in \{1, 2\}$  (the coordinate index), find  $\vec{\mathcal{V}}^{i(j)} \in \mathbf{H}_0^1(Y)$  satisfying (in the distributional sense)

$$\begin{aligned} \nabla \cdot (\mathbb{A} \mathbf{e}(\vec{\mathcal{V}}^{i(j)})) &= 0, \quad \text{in } Y_1^0 \cup Y_2^0, \\ \vec{\mathcal{V}}^{i(j)} &= 0, \quad \text{on } \partial Y, \\ \vec{\mathcal{V}}^{i(j)}(y(t)) &= \boldsymbol{\delta}^{(j)} \bar{B}_{i,p}(t) \quad \text{for } y(t) \in \Gamma_{12}^0, 0 \leq t < n, \end{aligned} \quad (18)$$

where  $\boldsymbol{\delta}^{(j)} = (\delta_k^{(j)}) = (\delta_{kj})$  and  $\mathbb{A} = (A_{ijkl})$  is the elasticity tensor of an artificial isotropic material. It is worth to remark that the reference domains  $Y_\beta^0$  can be updated during the optimization process, see Section 6.

## 4.2 Constraints

The size of the band gaps, expressed with objective function (14), can be easily enlarged by increasing the inclusion size, see Section 3 about scaling or numerical results [39]. Therefore, we discuss here the possible constraints that limits the inclusion size.

- Although the optimization criterion concerns with the band gap, thus, with the wave propagation phenomena, the material itself can be exposed independently to other types of static

---

<sup>6</sup>Domains  $Y_\beta^0$  are introduced in the context of FE mesh used for the numerical solutions. The so-called remeshing is accomplished using fields  $\vec{\mathcal{V}}^i = (\mathcal{V}_j^i)$  computed by solving (18).



loads. Therefore, also the effective material stiffness can be subject of some additional requirements. Obviously, the change in shape of the inclusions may lead to a very compliant material, or even to a loss of material integrity; as an example in Section 3.2 we demonstrated, how such effects can be provoked by the desired increase in bang-gap size by means of increasing the inclusion size. Therefore, it is natural to require some minimum material stiffness. For this we define the tensor  $\mathbb{D}_{\min}$  which represents admissible effective elastic properties (8), and require

$$[\mathbb{D}(\boldsymbol{\alpha})\mathbf{e}] : \mathbf{e} \geq [\mathbb{D}_{\min}\mathbf{e}] : \mathbf{e} > 0 \quad \text{for any macroscopic strain } \mathbf{e} \in \mathbb{R}_{\text{sym}}^{d \times d}. \quad (19)$$

- Alternatively, the constraint on a volume fraction  $|Y_2(\boldsymbol{\alpha})|/|Y| = \bar{\phi}$  can be considered. Although it can lead to the loss of material integrity, it has an engineering importance, as it corresponds to both the change of mass and a construction price.

In the optimization problem treated in the rest of the paper we account for the elasticity constraint (19), but disregard any volume constraint.

### 4.3 Setting the optimization problem

Here, we formulate and discuss an optimization problem, which arise as a combination of the objective function for band gap size (14) and the constraints (19) from previous section.

$$\min_{\boldsymbol{\alpha} \in \mathcal{A}} -\Phi_k(\boldsymbol{\alpha}) \quad (20a)$$

$$\text{s.t. } (\mathbb{D}(\boldsymbol{\alpha}) - \mathbb{D}_{\min})\mathbf{e} : \mathbf{e} \geq 0 \quad \forall \mathbf{e} \in \mathbb{R}_{\text{sym}}^{2 \times 2}. \quad (20b)$$

Problem (20a) has a complicated structure because of the evaluation of the objective function value, as explained using Algorithm 1. It involves the design parameters  $\boldsymbol{\alpha}$  and the state variables: the objective function depends on the spectrum  $(\lambda^r, \boldsymbol{\varphi}^r)$ ,  $r \in \mathcal{R}$ , whereas the elasticity constraint depends on the characteristic elastic response  $\mathbf{w}^{ij} \in \mathbf{H}_{\#}^1(Y)$ .

---

**Algorithm 1** Calculation of band gap size in continuous setting

---

**Require:** Control points  $\mathbf{P}^i$  for  $i = 0, \dots, n-1$  of B-spline, index  $k \in \mathbb{N}$  of band gap

- 1: **procedure** BAND GAP-SIZE:  $\Phi_k(\boldsymbol{\alpha})$
  - 2:   Set the domains  $Y_1 = Y_1(\boldsymbol{\alpha})$  and  $Y_2 = Y_2(\boldsymbol{\alpha})$
  - 3:   Calculate eigenvalue problem (4) for  $(\lambda_h^r, \boldsymbol{\varphi}_h^r) \in \mathbb{R} \times \mathbf{H}_0^1(Y_2)$  with  $r \in \mathbb{N}$
  - 4:   Calculate eigenmomentum  $\mathbf{m}^r = \int_{Y_2} \boldsymbol{\varphi}^r$  and average density  $\langle \rho \rangle = \sum_{k=1,2} \int_{Y_k} \rho^k$ .
  - 5:   Calculate the relevant spectrum with the index set  $\mathcal{R} \subset \mathbb{N}$  in accordance with (6)
  - 6:   Calculate  $\omega_k^r \in \Lambda_k$  using (10) such that  $r$ -th eigenvalue of  $M(\omega_k^r)$  is zero
  - 7: **end procedure: return**  $\Phi_k(\boldsymbol{\alpha}) = \omega_k^r(\boldsymbol{\alpha}) - \sqrt{\lambda^k(\boldsymbol{\alpha})}$  ▷ band gap size
- 

For clarity, we introduce the following detailed formulation which brings explicitly relationships between the state variables involved in the problem on one hand, and the constraints, on the other

hand:

$$\begin{aligned} & \min_{\boldsymbol{\alpha} \in \mathcal{A}} -\Phi_k(\omega_k^1(\boldsymbol{\alpha}), \lambda^k(\boldsymbol{\alpha})) \\ \text{s.t. } & \begin{cases} (i) & (\lambda^r, \boldsymbol{\varphi}^r), r \in \mathcal{R} \text{ given by the eigenvalue problem (4) ,} \\ (ii) & \omega_k^1 \text{ solves (11) ,} \\ & \text{where } (\lambda^r, \boldsymbol{\varphi}^r) \mapsto \mathbf{M}(\cdot) \text{ is defined by (7) ,} \\ (iii) & \text{the elasticity constraint (19) ,} \\ & \text{where } (\mathbf{w}^{ij}) \mapsto \mathbb{D} \text{ is defined by (8b), (8a) .} \end{cases} \end{aligned} \quad (21)$$

We now discuss several aspects of the optimization problem (21).

1. The evaluation of elastic constraint (19) or (20b) requires calculation of effective elastic properties  $\mathbb{D}(\boldsymbol{\alpha})$  from (8) and calculation of the smallest eigenvalue for  $(\mathbb{D}(\boldsymbol{\alpha}) - \mathbb{D}_{\min})$ , which has to be nonnegative.
2. Note that  $\boldsymbol{\alpha} \mapsto Y_2$ , therefore  $\boldsymbol{\alpha} \mapsto (\lambda^r, \boldsymbol{\varphi}^r)$ ,  $r \in \mathcal{R}$  and  $\boldsymbol{\alpha} \mapsto (\mathbf{w}^{ij})$ . This dependence is explained in detail in Section 5.
3. The sensitivity analysis of the objective function  $\Phi_k$  does not necessitate any adjoint problem to be solved. In a case of eigenvalues with multiplicity higher than one, only a subgradient of  $\Phi_k$  exists.
4. Although the stiffness constraint is associated with the state problem variable  $(\mathbf{w}^{ij})$ , there is no need to introduce an adjoint variable to compute the sensitivity.

## 5 Sensitivity analysis

In order to use a gradient-based optimization method, the sensitivity analysis associated with the optimization problem (20) is needed. Therein, the implicit dependence of  $\hat{\omega}_k(\boldsymbol{\alpha})$ ,  $\lambda^k(\boldsymbol{\alpha})$  and  $\mathbb{D}(\boldsymbol{\alpha})$  on the optimization variables  $(\boldsymbol{\alpha})$  can be understood by virtue of the unfolded formulation (21).

The aim of this section is to derive the sensitivity formulas which are needed to compute the gradient  $\nabla_{\boldsymbol{\alpha}} \Phi(\boldsymbol{\alpha}) = (\partial \Phi(\boldsymbol{\alpha}) / \partial \alpha_j^i)$  of objective function  $\Phi(\boldsymbol{\alpha})$  computed according the Algorithm 1; the gradient of the constraint involving elastic properties  $\mathbb{D}(\boldsymbol{\alpha})$  is given separately in Bby formula (40). We follow the standard approach based on the concept of the shape and material derivatives; for all details on this issue we refer to [17] and [16, 15]. To associate a locally perturbed shape with a shifted “material point” position defined for any  $y \in Y$ , the design velocity field  $\vec{\mathcal{V}}$  is introduced, such that

$$z_i(y, \tau) = y_i + \tau \mathcal{V}_i(y), \quad i = 1, 2, \quad (22)$$

where  $\tau$  is the “time-like” variable; here we use the design velocity field  $\vec{\mathcal{V}}$  in much the same sense as the one introduced in (17), where it was associated with particular design variables  $\alpha_j^i$ .

Throughout the text below we shall use the notion of the following derivatives:

$$\begin{aligned} \delta(\cdot) & \dots \text{ total (material) derivative} \\ \delta_{\tau}(\cdot) & \dots \text{ partial (shape) derivative w.r.t. } \tau \text{ in the context of (22) .} \end{aligned}$$

These derivatives are computed as the directional derivatives in the direction of  $\vec{\mathcal{V}}(y)$ ,  $y \in Y$ , see e.g. [15] for the classical results. In this paper we use  $\vec{\mathcal{V}} \in \mathbf{H}_0^1(Y)$ , so that  $\partial Y$  is not being perturbed.

Below we derive formulas needed to compute  $\delta \Phi$  for any  $\vec{\mathcal{V}}$ . Consequently,  $\partial \Phi(\boldsymbol{\alpha}) / \partial \alpha_j^i$  is evaluated using  $\delta \Phi$  where one substitutes  $\vec{\mathcal{V}} = \vec{\mathcal{V}}^{i(j)}$ , see (17).

## 5.1 Sensitivity of the spectrum

The problem of shape sensitivity of eigenvalues and eigenvectors  $(\lambda^r, \varphi^r)$  for  $r \in \mathcal{R}$  is discussed exhaustively e.g. in [17]. Here we introduce the sensitivity for the case of single, separated eigenvalues, i.e.  $\lambda^r \neq \lambda^s$  for any  $r, s \in \mathcal{R}$ . In such a situation, all elements  $(\lambda^r, \varphi^r)$  for  $r \in \mathcal{R}$  are differentiable with respect to  $\tau$ .

**Remark 5.** (*Multiple eigenvalues of  $M(\omega)$* ) On the other hand, a more complex treatment is required for situations with eigenvalues of higher multiplicities; then only the directional shape differentials exists. It should be emphasized that optimal solutions may often be featured by multiple eigenvalues; in the context of our problem such situation would emerge for spherical inclusions or some other symmetric shapes, see e.g. discussion in paper [4].

△

For brevity in what follows we employ following notation

$$a_{Y_2}(\mathbf{u}, \mathbf{v}) = \int_{Y_2} [\bar{\mathbf{C}}^2 \mathbf{e}^y(\mathbf{u})] : \mathbf{e}^y(\mathbf{v}), \quad \varrho_{Y_2}(\mathbf{u}, \mathbf{v}) = \int_{Y_2} \rho^2 \mathbf{u} \cdot \mathbf{v}. \quad (23)$$

In analogy we define  $a_{Y_1}(\mathbf{u}, \mathbf{v})$  using  $Y_1$  and the elasticity tensor  $\mathbf{C}^1$ .

The spectral problem (4) can be rewritten using the notation introduced above,

$$\varphi^k \in \mathbf{H}_0^1(Y_2), \quad a_{Y_2}(\varphi^k, \mathbf{v}) = \lambda_k \varrho_{Y_2}(\varphi^k, \mathbf{v}) \quad \forall \mathbf{v} \in \mathbf{H}_0^1(Y_2), \quad \varrho_{Y_2}(\varphi^k, \varphi^j) = \delta_{kj} \quad (24)$$

Differentiation of (24) yields

$$a_{Y_2}(\delta \varphi^r, \mathbf{v}) - \lambda_r \varrho_{Y_2}(\delta \varphi^r, \mathbf{v}) = \delta \lambda_r \varrho_{Y_2}(\varphi^r, \mathbf{v}) + \lambda_r \delta_\tau \varrho_{Y_2}(\varphi^r, \mathbf{v}) - \delta_\tau a_{Y_2}(\varphi^r, \mathbf{v}), \quad (25)$$

to be satisfied for all  $\mathbf{v} \in \mathbf{H}_0^1(Y_2)$ . Due to  $\delta \varphi^r \in \mathbf{H}_0^1(Y_2)$ , the l.h.s. of (25) vanishes for  $\mathbf{v} = \varphi^r$  so that we have the sensitivity of the  $r$ -th eigenvalue (recall the ortho-normality  $\varrho_{Y_2}(\lambda_r, \lambda_k) = \delta_{rk}$ ):

$$\delta \lambda_r = \delta_\tau a_{Y_2}(\varphi^r, \varphi^r) - \lambda_r \delta_\tau \varrho_{Y_2}(\varphi^r, \varphi^r). \quad (26)$$

The shape derivative  $\delta \varphi^r$  can be projected to the Hilbert space constituted by all eigenfunctions  $\{\varphi^k\}_k, k \geq 1$ . For this the Fourier coefficients are needed:

$$\xi_k^r = \varrho_{Y_2}(\delta \varphi^r, \varphi^k), \quad k = 1, 2, \dots, \quad \text{so that } \delta \varphi^r = \sum_{k \geq 1} \xi_k^r \varphi^k. \quad (27)$$

Now the l.h.s. in (25) can be written in the form

$$a_{Y_2}(\delta \varphi^r, \mathbf{v}) - \lambda_r \varrho_{Y_2}(\delta \varphi^r, \mathbf{v}) = \sum_{k \geq 1} (\lambda_k - \lambda_r) \varrho_{Y_2}(\varphi^k, \mathbf{v}) \xi_k^r. \quad (28)$$

Clearly (28) and also the first right hand side term in (25) vanish for  $\mathbf{v} = \varphi^r$  or for  $k = r$ . Therefore, from (25) and (28) we can obtain  $\delta \varphi^r$  up to a multiple of  $\varphi^r$ . Using the Fourier coefficients  $\xi_k^r$  and for any  $\varphi^s \neq \varphi^r$  these two equalities yield

$$\sum_{k \geq 1, k \neq r} \xi_k^r (\lambda_k - \lambda_r) \varrho_{Y_2}(\varphi^k, \varphi^s) = \lambda_r \delta_\tau \varrho_{Y_2}(\varphi^r, \varphi^s) - \delta_\tau a_{Y_2}(\varphi^r, \varphi^s)$$

and thus we have for  $s \neq r$

$$\xi_s^r = \frac{\lambda_r \delta_\tau \varrho_{Y_2}(\boldsymbol{\varphi}^r, \boldsymbol{\varphi}^s) - \delta_\tau a_{Y_2}(\boldsymbol{\varphi}^r, \boldsymbol{\varphi}^s)}{\lambda_s - \lambda_r} . \quad (29)$$

In order to determine  $\xi_r^r$ , we differentiate the identity  $\varrho_{Y_2}(\boldsymbol{\varphi}^r, \boldsymbol{\varphi}^r) = 1$ , thus, we get

$$\xi_r^r = -\frac{1}{2} \delta_\tau \varrho_{Y_2}(\boldsymbol{\varphi}^r, \boldsymbol{\varphi}^r) . \quad (30)$$

Now  $\delta \boldsymbol{\varphi}^r$  can be evaluated by (27)<sub>2</sub>. The partial shape derivatives  $\delta_\tau a_{Y_2}(\cdot, \cdot)$ ,  $\delta_\tau \varrho_{Y_2}(\cdot, \cdot)$  are given in Bby expressions (39).

## 5.2 Sensitivity of the homogenized mass tensor $\mathbf{M}$

Total variation of components  $M_{ij}$  defined in (7) yields

$$\delta M_{ij} = \partial_\omega M_{ij} \delta \omega + \sum_{r \in \mathcal{R}} (\partial_{\lambda_r} M_{ij} \delta \lambda_r + \partial_{\mathbf{m}^r} M_{ij} \cdot \delta \mathbf{m}^r) + \delta_\tau \langle \rho \rangle \delta_{ij} , \quad (31)$$

where  $\partial_{\mathbf{m}^r} = (\partial_{m_i^r}) = (\partial / \partial m_i^r)$ . Above we need the partial derivatives:

$$\partial_\omega M_{ij} = \frac{2}{\omega} (M_{ij} - \langle \rho \rangle \delta_{ij}) + \sum_{r \in \mathcal{R}} \frac{2\omega^3}{(\omega^2 - \lambda_r)^2} m_i^r m_j^r , \quad (32)$$

$$\partial_{\lambda_r} M_{ij} = -\frac{\omega^2}{(\omega^2 - \lambda_r)^2} m_i^r m_j^r , \quad (33)$$

$$\partial_{\mathbf{m}^r}^k M_{ij} = -\frac{\omega^2}{\omega^2 - \lambda_r} (\delta_{ki} m_j^r + \delta_{kj} m_i^r) . \quad (34)$$

In (31) we need the sensitivity of the eigenmomentum  $\mathbf{m}^r$ . The sensitivity  $\delta \boldsymbol{\varphi}^r$  is given by (27)<sub>2</sub> involving the coefficients  $\xi_s^r$ , see (29),(30) which depend on the shape derivatives introduced in (39), B. By virtue of (39)<sub>2</sub> it is easy to get

$$\delta \mathbf{m}^r = \rho^2 \int_{Y_2} \left( \delta \boldsymbol{\varphi}^r + \boldsymbol{\varphi}^r \nabla \cdot \vec{\mathcal{V}} \right) . \quad (35)$$

The partial shape derivative  $\partial_\tau \langle \rho \rangle$  is given by (39)<sub>3</sub>.

## 5.3 Sensitivity of the upper band gap bound $\omega_k^r$

The upper bound of the phononic gap is defined above in (11). We derive the sensitivity formula for any index  $r$  such that the root  $\omega_k^r$  exists (in particular, we rely on the existence of  $\omega_k^1$ ) within the interval  $\Lambda_k$ . By virtue of (10), using (31) and assuming  $\gamma^r(\omega_k^r)$  has multiplicity one <sup>7</sup>, it is easy to find

$$\partial \gamma^r(\omega_k^r) = (\mathbf{v}^r)^T \partial \mathbf{M}(\omega_k^r) \mathbf{v}^r .$$

---

<sup>7</sup>This assumption is consistent with the isolated spectrum,  $\lambda^i \neq \lambda^j$  for  $i \neq j$ .

Sensitivity of  $\omega_k^r$  now follows from (11) on substituting from (31). We get

$$\begin{aligned} 0 &\stackrel{!}{=} \partial \gamma^r(\mathbf{M}(\omega_k^r)) = (\mathbf{v}^r)^T (\partial \mathbf{M}(\omega_k^r)) \mathbf{v}^r \\ &= x_j^r \left( \partial_\omega M_{ij}(\omega_k^r) \delta \hat{\omega} + \sum_{r \in \mathcal{R}} (\partial_{\lambda_r} M_{ij}(\omega_k^r) \delta \lambda_r + \partial_{\mathbf{m}^r} M_{ij}(\omega_k^r) \cdot \delta \mathbf{m}^r) + \delta_\tau \langle \rho \rangle \delta_{ij}(\omega_k^r) \right) x_j^r, \end{aligned}$$

where all functions involved are evaluated at  $\omega_k^r$ , hence

$$\delta \omega_k^r = - \frac{1}{(\mathbf{v}^r)^T \partial_\omega \mathbf{M}(\omega_k^r) \mathbf{v}^r} x_j^r \left( \sum_{r \in \mathcal{R}} (\partial_{\lambda_r} M_{ij}(\omega_k^r) \delta \lambda_r + \partial_{\mathbf{m}^r} M_{ij}(\omega_k^r) \cdot \delta \mathbf{m}^r) + \delta_\tau \langle \rho \rangle \delta_{ij}(\omega_k^r) \right) x_j^r,$$

To evaluate  $\delta \omega_k^r$ , the expressions (26), (32), (35) are employed. The partial shape derivatives  $\delta_\tau \langle \rho \rangle$  is computed using expression (39)<sub>3</sub> given in B.

## 6 Discretization, implementation, and numerical optimization

In this section, we focus on discretization and implementation of equations presented in previous sections. Particularly, in Section 6.1, the discretization and implementation is briefly presented with an emphasis on the algorithmic framework that was used to calculate and optimize band gaps. The initial problems are presented in 6.2 while Sections 6.3 and 6.4 deal with numerical examples.

### 6.1 Discretization and implementation

Here, we briefly describe discretization and implementation of equations leading to calculation and optimization of band gaps. For discretization, Finite element method (FEM) based on Galerkin approximation was used with triangular elements and linear polynomials as basis functions. Hence, all the function spaces such as  $\mathbf{H}_0^1(Y_1)$  are approximated by corresponding discrete ones  $\mathbb{H}_{0,h}^1(Y_{1,h})$  with discretization parameter  $h$  corresponding to a characteristic mesh size. The domains  $Y_{1,h}(\boldsymbol{\alpha})$  or  $Y_{2,h}(\boldsymbol{\alpha})$  are also mesh dependent because the smooth B-spline inclusion boundary  $\Gamma(\boldsymbol{\alpha})$  is approximated with polygon  $\Gamma_h(\boldsymbol{\alpha})$  during meshing, however still satisfying  $Y_{1,h}(\boldsymbol{\alpha}) \cap Y_{2,h}(\boldsymbol{\alpha}) \cap \Gamma_h(\boldsymbol{\alpha}) = Y$  and  $Y_{1,h}(\boldsymbol{\alpha}) \cup Y_{2,h}(\boldsymbol{\alpha}) = \emptyset$ . Then, also all variables, such as  $\lambda_h^k, \varphi_h^k, \omega_{k,h}^1, \mathbf{M}_h(\omega)$  occurring during optimization, are mesh dependent. To simplify notation, we omit the discretization parameter  $h$  from variables and also approximation spaces  $\mathbb{H}_0^1(Y_1)$ .

For implementation, the following packages were utilized:

- Implementation of band gap calculation was provided with FEniCS project, which is a collection of free software with an extensive list of features for automated, efficient solution of differential equations, see [23, 1].
- The computational domain of periodic cell  $Y$  was discretized with a finite element mesh using software package Gmsh described in [14]. Noting that the B-spline, which separates the domain  $Y$  into two parts (inclusion and matrix), was approximated by a polygon.
- Optimization itself was calculated within an open-source software PyOpt, described in [31], which is a Python-based package for formulating and solving nonlinear constrained optimization problems in an efficient, reusable and portable manner. As an optimization algorithm, Sequential Least Squares Programming (SLSQP) was utilized [20].

Now, the discrete optimization problem arises from the general one in (20a)

$$\min_{\boldsymbol{\alpha} \in \mathbb{R}^{2 \times (n-1)}} -\Phi_k(\boldsymbol{\alpha}), \quad \text{the band gap size,} \quad (36a)$$

$$\text{s.t. } |\alpha_i^j| \leq \alpha^{\max} = 0.05 \text{ for all } i, j, \quad \text{constraint on design variables.} \quad (36b)$$

$$\begin{aligned} D_{1111}(\boldsymbol{\alpha}) &\geq D_{1111}^{\min} = 24 \text{ GPa,} \\ D_{2222}(\boldsymbol{\alpha}) &\geq D_{2222}^{\min} = 24 \text{ GPa,} \\ D_{1212}(\boldsymbol{\alpha}) &\geq D_{1212}^{\min} = 8 \text{ GPa,} \end{aligned} \quad \text{constraint on elastic properties,} \quad (36c)$$

Compared to (20a), the major modification is not only in formulation with discrete spaces but also in constraints:

- The evaluation of objective function  $\Phi_k$  is provided by Galerkin approximation framework with discrete FEM spaces, compare Algorithm 1 with Algorithm 2.
- The major complexity arises from the need of computing the whole spectrum of the eigenvalue problem (38) but also from the sensitivity for all eigenvectors. The computational costs are reduced by omitting non-relevant frequencies. For some threshold value  $\theta$ , a criterion can be based on the norm of eigenmomentum  $|\mathbf{m}^r| > \theta$ . Here, since we calculate band gaps or eigenvalues of  $\mathbf{M}(\omega)$  only in  $[\sqrt{\lambda^k}, \sqrt{\lambda^{k+1}}]$ , we propose the following criterion modification leading to index set of relevant spectrum

$$R_\theta = \{r \in \mathbb{N} : r \leq \dim \mathbb{H}_h(Y_2) \text{ and } \left| \frac{\bar{\omega}_k^2}{\bar{\omega}_k^2 - \lambda_h^r} \right| \cdot |\mathbf{m}^r|^2 > \theta\} \text{ for } \bar{\omega}_k^2 := \frac{\lambda^k + \lambda^{k+1}}{2} \quad (37)$$

this term occurs in mass matrix and its value rapidly decreases for an increase in the distance from investigated band gap.

- The constraint on effective elastic coefficients (19), namely  $(\mathbb{D} - \mathbb{D}_{\min})\mathbf{e} : \mathbf{e} \geq 0$  for all  $\mathbf{e} \in \mathbb{R}_{\text{sym}}^{2 \times 2}$ , leads to the constraint on the eigenvalues of  $\mathbb{D}$ . Here, we simplify the constraint by testing only with loads in principal directions  $\begin{pmatrix} 1 & 0 \\ 0 & 0 \end{pmatrix}$ ,  $\begin{pmatrix} 0 & 0 \\ 0 & 1 \end{pmatrix}$ , and shear  $\begin{pmatrix} 0 & 1 \\ 1 & 0 \end{pmatrix}$ , which results in constraints on  $D_{1111}$ ,  $D_{2222}$ , and  $D_{1212}$ , respectively. Since the test loads span the space of symmetric matrices, it still satisfies some minimal stiffness for any load, however, it lacks the invariance with respect to rotations. As a consequence, the optimal shapes have a predominant orientation, see Sections 6.3 and 6.4.
- The constraint on design variables  $\boldsymbol{\alpha} \in \mathbb{R}^{2 \times (n-1)}$  is incorporated in (36b) to keep the sufficient quality of the mesh and to satisfy a good meaning of domains and boundaries, see (15). However, this constraint is neither sufficient nor optimal. Therefore, the quality of the mesh is also controlled to indicating for the admissibility of an inclusion shape, see (15).

Because of the last point, the optimization algorithm SLSQP may fail to converge or the solution is suboptimal due to strong restriction on design variables  $\boldsymbol{\alpha}$ . Therefore, we have incorporated adaptive procedure presented in Algorithm 3. It updates the B-spline points when the suboptimal solution is reached, which allow for better optimization results. It also controls the quality of mesh indicating the admissibility of the design variables; when needed, the parameters in discrete optimization problem (36) can be adjusted.

Since the SLSQP belongs to gradient-based optimization algorithms, the gradient of objective function is implemented and presented in Algorithm 4. This is also provided for the evaluation of elastic constraint and its gradient in Algorithm 5.

---

**Algorithm 2** Calculation of weak band gap size in discrete setting

---

**Require:** Control points  $\mathbf{P}^i$  for  $i = 0, \dots, n-1$  of B-spline, index  $k \in \mathbb{N}$  of band gap, a corresponding FEM mesh, design velocities  $\mathcal{V}^{i(j)}$ , threshold  $\theta$  for (37)

- 1: **procedure** OBJECTIVE-FUNCTION(FEM mesh,  $\alpha$ ,  $\mathcal{V}^{i(j)}$ ,  $\theta$ ) ▷ band gap size
- 2:   Set  $Y_1 = Y_1(\alpha)$  and  $Y_2 = Y_2(\alpha)$  by updating the FEM mesh using  $\alpha$  and  $\mathcal{V}^{i(j)}$
- 3:   Calculate eigenelements  $(\lambda^r, \varphi^r) \in \mathbb{R} \times \mathbb{H}_0^1(Y_2)$ ,  $r = 1, 2, \dots, \dim \mathbb{H}_0^1(Y_2)$  of the Galerkin approximation to the eigenvalue problem (4)

$$\int_{Y_2} [\mathbf{C}^{\text{phys}} e^y(\varphi^r)] : e^y(\mathbf{v}) = \lambda^r \int_{Y_2} \rho^2 \varphi^r \cdot \mathbf{v} \quad \forall \mathbf{v} \in \mathbb{H}_0^1(Y_2), \quad \int_{Y_2} \rho^2 \varphi^r \cdot \varphi^s = \delta_{rs} \quad (38)$$

- 4:   Calculate eigenmomentum  $\mathbf{m}^r = \int_{Y_2} \varphi^r$  and average density  $\langle \rho \rangle = \sum_{k=1,2} \int_{Y_k} \rho^k$ .
  - 5:   Calculate the relevant spectrum using the index set  $\mathcal{R}_\theta$  in accordance with (37)
  - 6:   Calculate  $\omega_k^1 \in ]\sqrt{\lambda^k}, \sqrt{\lambda^{k+1}}[$  using (10), i.e. the smallest eigenvalue  $\gamma^1(\omega_k^1)$  of approximated mass matrix  $\mathbf{M}(\omega^2) = \langle \rho \rangle \mathbf{I} - \frac{1}{|Y|} \sum_{r \in R_\theta} \frac{\omega^2}{\omega^2 - \lambda^r} \mathbf{m}^r \otimes \mathbf{m}^r$  is zero
  - 7: **end procedure: return**  $\Phi_k(\alpha) = \omega_k^1(\alpha) - \sqrt{\lambda^k(\alpha)}$
- 

---

**Algorithm 3** Overall optimization algorithm of band gap size

---

**Require:** Control points  $\mathbf{P}^i$  for  $i = 0, \dots, n-1$  of B-spline, index  $k \in \mathbb{N}$  of band gap, a discretization parameter  $h$ , threshold  $\theta$  for (37)

- 1: **repeat**
  - 2:   Generate a FEM mesh dependent on  $\mathbf{P}^i$  and discretization parameter  $h$
  - 3:   Calculate design vel.  $\mathcal{V}^{i(j)}$  using Galerkin approximation of auxiliary problem (18)
  - 4:   Calculate  $\alpha_{\text{opt}}^i$  of discrete optimization problem (36) using SLSQP algorithm  
    ▷ Use here Alg. 2,4, 5 for evaluation of obj. function, constraint, and their gradients
  - 5:   **if** SLSQP converged and the quality of mesh is in tolerance **then**
  - 6:      $\mathbf{P}^i \leftarrow \mathbf{P}^i + \alpha_{\text{opt}}^i$  ▷ Update of B-spline control points with an optimal solution
  - 7:   **else**
  - 8:     Stop or adjust parameters of the discrete optimization problem (36)
  - 9:   **end if**
  - 10: **until** The size of band gap increases
  - 11: **return** Admissible topology with highest band gap size
- 

---

**Algorithm 4** Calculation of gradient of band gap size w.r.t. design variables

---

**Require:** Requirements as in Algorithm 2 and its auxiliary results such as eigenelements  $(\lambda^r, \varphi^r)$  for  $r \in \mathcal{R}_\theta$ , upper bound of band gap  $\omega_k^1$ , average density  $\langle \rho \rangle$ , eigenmoments  $\mathbf{m}^r$

- 1: **procedure** GRAD-OBJECTIVE-FUNCTION(FEM mesh,  $\alpha$ ,  $\mathcal{V}^{i(j)}$ )
  - 2:   Set  $Y_1 = Y_1(\alpha)$  and  $Y_2 = Y_2(\alpha)$  by updating the FEM mesh using  $\alpha$  and  $\mathcal{V}^{i(j)}$
  - 3:   **for all** design velocities  $\mathcal{V}^{i(j)}$  **do**
  - 4:     Calculate sensitivity to eigenelements  $(\lambda^r, \varphi^r)$  for  $r \in R_\theta$  using (26) and (27)
  - 5:     Calculate the sensitivity of mass matrix  $\mathbf{M}(\omega_k^1)$  according to Section 5.2
  - 6:     Calculate the sensitivity of eigenvalues of mass matrix  $\mathbf{M}(\omega_k^1)$
  - 7:   **end for**
  - 8: **end procedure: return**  $\nabla_\alpha \Phi_k(\alpha) = \nabla_\alpha \omega_k^1(\alpha) - \nabla_\alpha \lambda^k(\alpha)$
-

---

**Algorithm 5** Elastic constraint and its gradient

---

**Require:** Requirements as in Algorithm 2

- 1: **procedure** ELASTIC-STIFFNESS(FEM mesh,  $\alpha$ ,  $\mathcal{V}^{i(j)}$ )
  - 2:   Set  $Y_1 = Y_1(\alpha)$  by updating the FEM mesh using  $\alpha$  and  $\mathcal{V}^{i(j)}$
  - 3:   Calculate corrector functions  $\mathbf{w}^{kl} \in \mathbb{H}_{\#}^1(Y_1)$  for  $k, l \in \{1, 2\}$  with Galerkin approximation of (8b)
  - 4:   Evaluate effective stiffness from (8a)
  - 5: **end procedure: return**  $\mathbb{D}(\alpha)$
  - 6: **procedure** GRAD-ELASTIC-STIFFNESS(FEM mesh,  $\alpha$ ,  $\mathcal{V}^{i(j)}$ ,  $\mathbf{w}^{kl}$ )
  - 7:   Set  $Y_1 = Y_1(\alpha)$  by updating the FEM mesh using  $\alpha$  and  $\mathcal{V}^{i(j)}$
  - 8:   **for all** design variables  $\mathcal{V}^{i(j)}$  **do**
  - 9:     Evaluate equation (40)
  - 10:   **end for**
  - 11: **end procedure: return**  $\nabla_{\alpha} \mathbb{D}(\alpha)$
-



## 6.2 Optimization problems

Here, we introduce and comment on problems and parameters that were used for numerical optimization, as described in previous Section 6.1. In Table 3, the material properties for both inclusion and matrix are presented together with an artificial elastic material used for the calculation of design velocities  $\mathcal{V}^{i(j)}$  in (18). Two types of inclusion, L-shaped and square-shaped, were used for optimization, see Figures 5 and 6 for both inclusion geometry with mesh and distribution of band gaps. The discretization parameters, such as number of mesh and spline nodes, are summarized in Table 6.2.

material	region	lame coef.	shear modulus	density
aluminium	matrix ( $Y_1$ )	$58.98 \cdot 10^9$ Pa	$26.81 \cdot 10^9$ Pa	$2.799 \cdot 10^3$ kg/m <sup>3</sup>
epoxy	inclusion ( $Y_2$ )	$1.798 \cdot 10^9$ Pa	$1.48 \cdot 10^9$ Pa	$1.142 \cdot 10^3$ kg/m <sup>3</sup>
auxiliary for $\mathcal{V}$	cell ( $Y$ )	$\frac{1}{2}$ Pa	1 Pa	—

Table 3: Material coefficients for optimization

Using the results about scaling of periodic cell or volume fraction in Section 3, we can confine the optimization on the unit cell with real material. It means that for the required stiffness, the optimal inclusion shape is independent of microstructure size. Its size can be evaluated a posteriori in order to obtain the band gap within required frequencies.

inclusion	Fig.	mesh vertices in $Y$	spline points	$\alpha^{\max}$	$D^{\min}$
L-shaped	5	2218	24	0.05	8 GPa
square	6	2153	24	0.05	8 GPa

Table 4: Discretization parameters for initial states;  $D^{\min} := D_{1212}^{\min} = \frac{1}{3} D_{1111}^{\min} = \frac{1}{3} D_{2222}^{\min}$

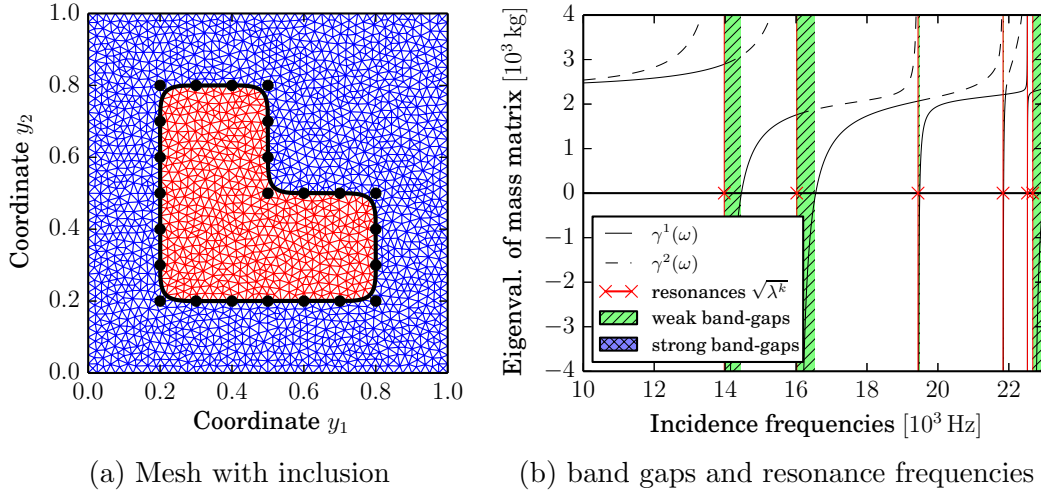


Figure 5: The initial state; (a) the mesh with red L-shaped inclusion, blue matrix, and black-doted spline boundary with black control nodes; (b) eigenvalues of mass matrix for incidence frequencies with weak band gaps and no strong band gaps

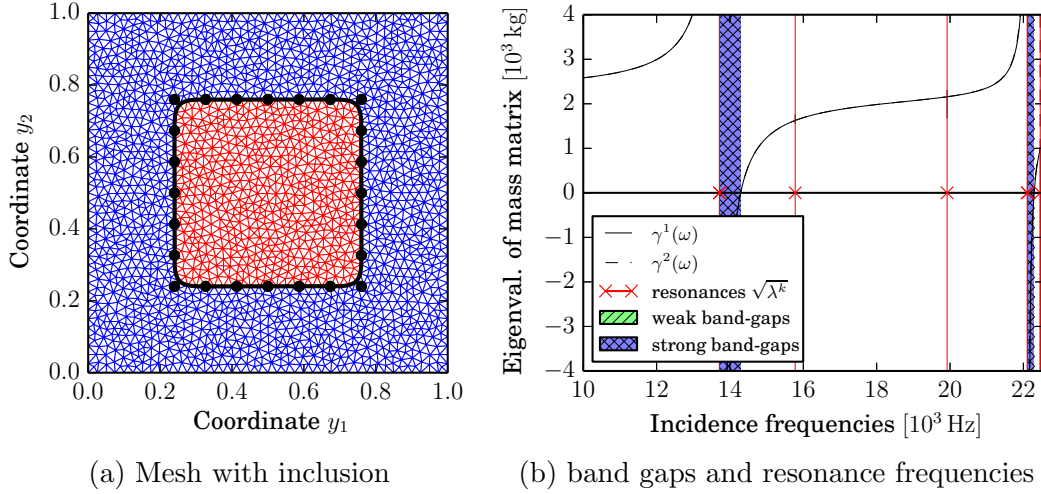


Figure 6: The initial state; (a) the mesh with blue matrix, red inclusion, and black-dotted spline boundary with black spline nodes; (b) eigenvalues of mass matrix for incidence frequencies with strong band gaps

### 6.3 Optimization of weak band gap in the first interval

Firstly, we focus on optimization of weak band gap size in the first interval  $[\sqrt{\lambda^1}, \sqrt{\lambda^2}]$ , because it converges without factual difficulties to optimal inclusion shape contrary to optimization in the second interval described in the following Section 6.4. Optimization of initial L-shaped inclusion shown Figure 5(a) leads to the optimal state, presented in Figure 7(a), which is characterized with an ellipse-like inclusion rotated by 45 degrees. The eigenvalues of mass matrix, distribution of band gaps, and resonance frequencies are depicted in Figures 5(b) and 6(b) for both initial geometries, while in Figure 7(b) for the optimal state.

The optimal design was obtained with three remeshing corresponding to three restarts of SLSQP algorithm. In the total values summarized in Table 5, the weak band gap size was enlarged about 89.5 %. It was accompanied with a significant increase in the inclusion size about 64.7 % in terms of the volume fraction  $|Y_2|/|Y|$ . However, there is also a significant decrease of effective elastic stiffness components  $D_{1111}$  and  $D_{2222}$  that corresponds to loads in axial directions; for the optimal shape, all elastic inequality constraints became active and are satisfied within the required tolerance. During optimization, the frequencies of band gap are also moved to lower absolute values, which can be compensated for by scaling with the size of periodic cell, see Section 3. Moreover, we also observe more resonance frequencies within a plotted area for optimal design than the initial state.

The evolution of band gap size during optimization is captured in Figure 8(a) together with constraint on shear component  $D_{1212}$  in Figure 8(b), which is the only constraint active during the whole optimization; the other two constraints also reaches their bound but only at the end. For each mesh (each call of SLSQP algorithm), the best improvement in band gap size is provided in the first iteration. Since that the approximate solutions escape the constraint admissible area; the consequent optimization is then focused on returning back to constraint admissible area within the required tolerance, which is reached at the last iteration. Moreover, the conforming method in primal formulation, used here, leads to the overestimation of the homogenized stiffness [46]; this can be avoided by using the dual formulation, easily with e.g. FFT-based homogenization [45].

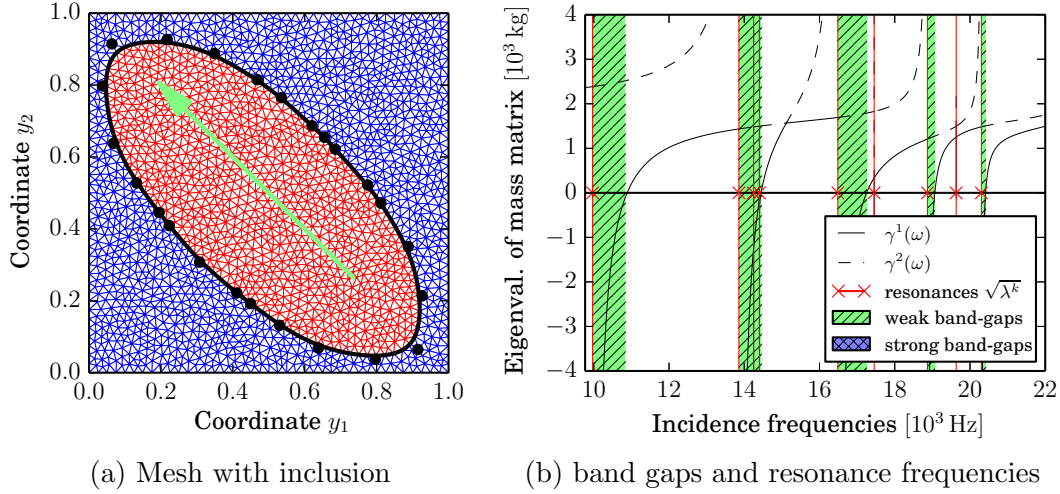


Figure 7: The optimal state for maximal weak band gap size in the first interval  $[\sqrt{\lambda^1}, \sqrt{\lambda^2}]$ , after 3 remeshing; (a) the mesh with blue matrix, red inclusion, and black boundary with spots of B-spline nodes; (b) eigenvalues of mass matrix for incidence frequencies, green denotes weak band gaps

inclusion	Fig.	$\Phi_1$	$\sqrt{\lambda^1}$	$\sqrt{\lambda^2}$	$\sqrt{\lambda^3}$	$D_{1111}$	$D_{2222}$	$D_{1212}$	$\frac{ Y_2 }{ Y }$
L-shape	5	0.484	13.975	16.021	19.439	42.334	42.335	8.147	0.266
optimal	7	0.917	9.969	13.857	14.249	23.998	23.998	7.997	0.438

Table 5: Optimization in first interval; the units are for band gap size  $\Phi_1$  and resonances  $\sqrt{\lambda^k}$  in [kHz], for effective elasticity  $\mathbf{ID}$  in [GPa], and for volume fraction  $\frac{|Y_2|}{|Y|}$  without unit

## 6.4 Optimization of weak band gap in the second interval

In this section, we describe the optimization of band gap size in second interval  $[\sqrt{\lambda^2}, \sqrt{\lambda^3}]$ . In previous section, the optimization in first interval led to the optimal design, but here the situation is more complicated. Therefore, we distinguish optimization of L-shape inclusion in Section 6.4.1 and square inclusion in Section 6.4.2, see Table 6.

### 6.4.1 Initial L-shape

The optimization of L-shape inclusion in Figure 5(a) leads to suboptimal state depicted in Figure 9, which is obtained after one remeshing, but with considering the constraints on maximal movement of spline nodes. When the remeshing is provided, the further optimization leads to topology/mesh collapse in the central area where the inclusion shape is concave. Here, the reformulation to topology optimization is of a great importance because spline parametrization can barely lead to more complicated inclusion topologies; in general, it is also difficult to provide reasonable constraints on a spline to avoid topology/mesh collapse.

### 6.4.2 Initial square-shape

For square-shape inclusion in Figure 6, a different inclusion topology and numerical difficulties are observed during optimization, which leads to the suboptimal inclusion shape in Figure 10. The

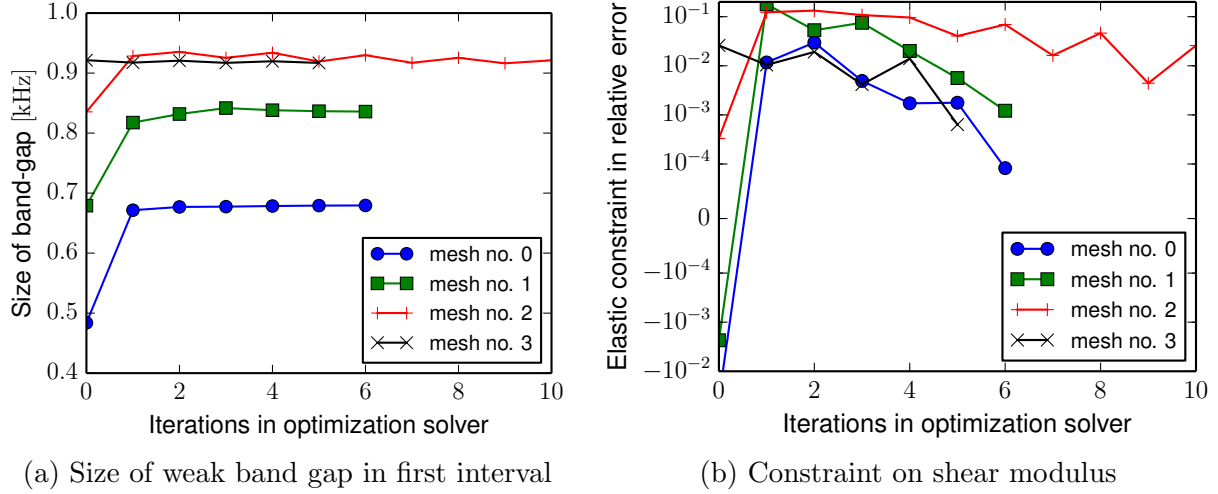


Figure 8: The evolution of (a) objective function  $\Phi_1(\alpha)$ , i.e. size of band gap in first interval, during optimization and (b) elastic constraint in relative error  $\frac{D_{1212}^{\min} - D_{1212}(\alpha)}{D_{1212}^{\min}}$ , negative values denotes admissible area; the convergence tolerance in SLSQP algorithm corresponds to  $10^{-3}$

inclusion	Fig.	$\Phi_2$	$\sqrt{\lambda^1}$	$\sqrt{\lambda^2}$	$\sqrt{\lambda^3}$	$D_{1111}$	$D_{2222}$	$D_{1212}$	$\frac{ Y_2 }{ Y }$
L-shaped	5	0.533	13.975	16.021	19.439	42.334	42.335	8.147	0.266
suboptimal	9	0.884	13.883	15.559	17.359	36.391	36.205	7.431	0.321
square	6	0.648	12.678	12.709	14.301	45.346	45.421	7.996	0.304
suboptimal	10	0.782	12.158	15.301	16.107	30.578	29.220	7.851	0.327

Table 6: Optimization in second interval; the units are for band gap size  $\Phi_2$  and resonances  $\sqrt{\lambda^k}$  in [kHz], for effective elasticity  $\mathbb{D}$  in [GPa], and for volume fraction  $\frac{|Y_2|}{|Y|}$  without unit

optimization was stopped here after three remeshing, because a 3rd eigenvalue border the upper bound of the weak band gap in second interval. It leads to numerical difficulties since the maximal eigenvalue of mass matrix goes to infinity at resonance frequency and the optimization algorithm allows for moving out from the constraint admissibility domain. Another optimization algorithms such as [47], which avoid movement from the admissible area, could be used here together with a constraint on a size of band gap with respect to the size of the corresponding interval  $\sqrt{\lambda^{k+1}} - \sqrt{\lambda^k}$ . We also note that since the initial state is symmetric with respect to main axis, it includes only blue-colored strong band gaps while the final state contains purely weak band gaps.

## 7 Conclusion

We presented a methodology for the optimization of phononic crystals with the main objective to maximize acoustic band-gaps. The band gap identification is based on the model of wave propagation in homogenized periodic strongly heterogeneous two-component materials which are featured by a high-contrast in the elastic coefficients. This modeling approach explained in [4, 38], cf. [2, 3], enables to determine the band gap bounds from the analysis of the homogenized mass (or the anisotropic effective density) tensor which depends on the frequency. Recall that this “metamaterial”

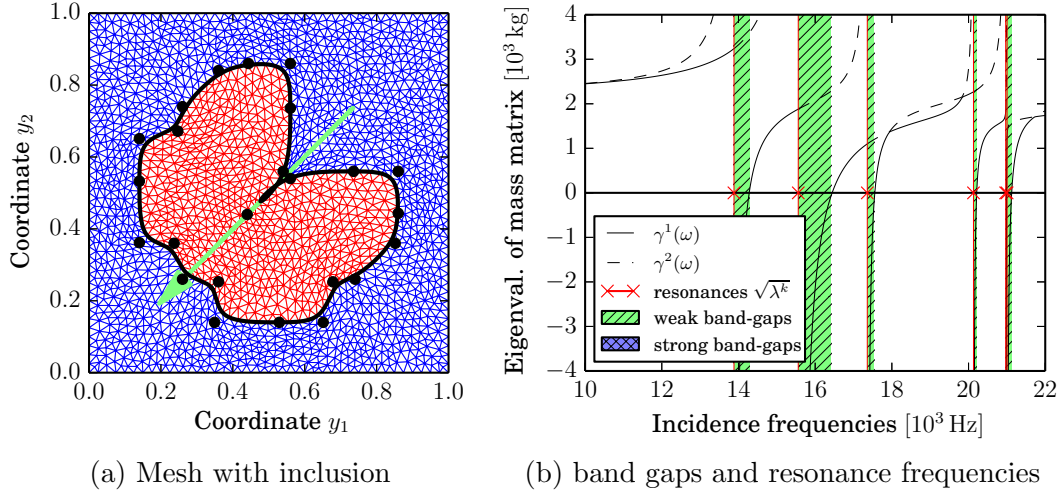


Figure 9: The optimal state for maximal weak band gap without remeshing (constrained on maximal spline node move)

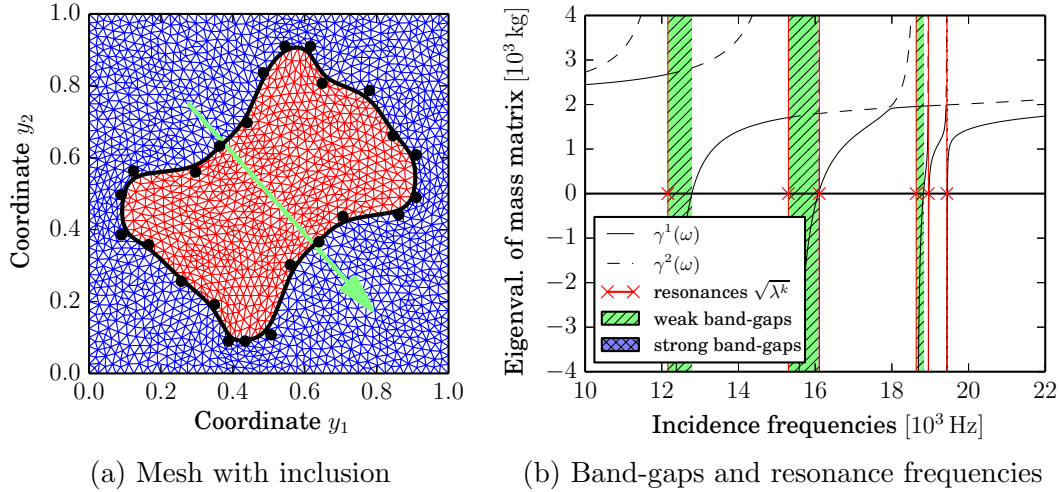


Figure 10: The optimal state for maximal weak band gap in first interval, after three remeshing; (a) the mesh with blue matrix, red inclusion, and black-dotted spline boundary with black spline nodes; (b) eigenvalues of mass matrix for incidence frequencies, green denotes weak band-gaps

rial” property of the model is relevant for situations when the wave length is significantly larger than the periodicity gauge of the phononic crystal which, thus, confines the range of frequencies considered for a given material components and the crystal size.

The most relevant results are now summarized:

- The optimization problem was formulated with weak band-gap size as objective function and minimum effective elasticity constraint, see Section 4.
- The size-effect of elastic wave propagation is described for a change of a microstructure size and for a change of inclusion size only, see Section 3. As a consequence, the behavior of the

model can be described only with an inclusion shape on a unit cell, i.e. with one forward calculation. However, the model is valid only for sufficiently small microstructure sizes, i.e. sufficiently smaller than the length of propagating waves.

- Numerical optimization of band-gaps is based on B-spline description of inclusion shape, discretization with FEM, and shape sensitivity with gradient-based optimization algorithm SLSQP. The complexity of the optimization problem is driven by the calculation of the whole spectral problem (4), and the sensitivity analysis of corresponding eigenvectors. In this respect, we also pursue an alternative approach of expressing the effective mass tensor which would allow to reduce the computational complexity.
- When optimized between the first two resonance frequencies, the optimal shape corresponds to an ellipse declined from the  $x_1$  axis by 45 degrees; this is a consequence of the constraint on elastic properties which lacks rotation-invariance, see Section 6.3.
- When optimized between the second two resonance frequencies, it results in the suboptimal geometries only; the convergence was stopped when the inclusion shapes lead to a collapse of the shape or when the band-gap filled the whole interval between two consecutive resonant frequencies.

As a difference to the classical approach which relies on the Bloch-Floquet theory, there is no need to search for the band gaps in the first Brillouin zone. In this context, our approach can distinguish strong band gaps, such that there are no propagating modes, or the weak band gaps which admit propagation of waves of certain polarizations only; this classification is independent of the direction of the wave propagation, as proved in [38].

We have focused on the shape optimization of 2D crystals consisting of the stiff matrix and a soft inclusion, the boundary of the latter being described by the cyclic B-spline. Due to the boundary smoothness guaranteed by the spline properties, we avoid the boundary oscillation associated with the spatial finite element discretization. For the objective function expressing a selected band gap length, the sensitivity analysis formulas has been derived so that gradient based method can be used to solve the optimization problem.

We observed that the form of the constraint imposed on the effective elasticity influences significantly the optimal shape. In this context it might be of practical interest to consider locally periodic structures with a moderate spatial variation of the inclusion shapes, *i.e.* with respect to the macroscopic position. Such a nonuniform phononic structure – a special type of the functionally graded material – would allow to achieve a locally optimized static stiffness and, simultaneously, to suppress undesired vibrations.

To avoid all difficulties arising in a case of nondifferentiable objective function, we confined to maximization of the weak band gaps which restrict the wave propagation only partially, for some polarizations (however, independently on the direction of the wave propagation). To handle also the strong band gaps, typically admitted by symmetric shapes of inclusions featured by resonant frequencies with higher multiplicity, the sensitivity analysis complicates and the nonsmooth optimization tools, like the bundle-type methods working with the notion of subdifferentials, must be resorted for. The sensitivity analysis of such a nonsmooth problem has been treated in [35] for piezo-phononic structures.

## A Transformation formulas for the size effect

We consider a given scale  $\varepsilon_0$ , such that  $\mathbf{C}^{\varepsilon_0} = \mathbf{C}^{\text{phys}}$  is the realistic value, see Remark 1. Let  $\varepsilon_1$  be another scale of the structure and define  $a = \frac{\varepsilon_1}{\varepsilon_0}$ . Further, by subscript  $(k)$  we label the quantities associated with the microstructure characterized by  $\varepsilon_k$ ,  $k = 1, 2$ . The following observations are straightforward:

- (i) the eigenfunctions are identical,  $\varphi_{(1)}^r = \varphi_{(0)}^r$  for  $r = 1, 2, \dots$ .
- (ii) By virtue of (4),  $\lambda_{(1)}^r$  computed for  $\bar{\mathbf{C}}_{(1)} := \varepsilon_{(1)}^{-2} \mathbf{C}^{\text{phys}} = \bar{\mathbf{C}}_{(0)} \left( \frac{\varepsilon_0}{\varepsilon_1} \right)^2 = a^{-2} \bar{\mathbf{C}}_{(0)}$  is related to  $\lambda_{(0)}^r$ , as follows:  $\lambda_{(1)}^r = \left( \frac{\varepsilon_0}{\varepsilon_1} \right)^{-2} \lambda_{(0)}^r = a^{-2} \lambda_{(0)}^r$ .
- (iii) Since  $\frac{\omega^2}{\omega^2 - \lambda_{(1)}^r} = \frac{a^2 \omega^2}{a^2 \omega^2 - \lambda_{(0)}^r}$ , the two effective mass tensors are equivalent for rescaled frequencies: it holds that  $\mathbf{M}_{(1)}(\omega) = \mathbf{M}_{(0)}(a\omega)$ .
- (iv) Due to the above observation (iii), the band gaps distributions are scaled by  $a$ . Let  $G_{(0)} = ]\underline{\omega}, \bar{\omega}[$ , then  $G_{(1)} = ]a^{-1}\underline{\omega}, a^{-1}\bar{\omega}[$ , thus,  $|G_{(1)}| = a^{-1}(\bar{\omega} - \underline{\omega}) = a^{-1}|G_{(0)}|$ .

## B Shape sensitivity – auxiliary results

By virtue of the shape sensitivity based on the domain parametrization [16], and using notation (23), the following formula hold,

$$\begin{aligned} \delta_\tau a_{Y_\beta}(\mathbf{u}, \mathbf{v}) &= \oint_{Y_\beta} C_{irks}^\beta \left( \delta_{rj} \delta_{sl} \nabla_y \cdot \vec{\mathbf{v}} - \delta_{jr} \partial_s^y \mathcal{V}_l - \delta_{ls} \partial_r^y \mathcal{V}_j \right) e_{kl}^y(\mathbf{u}) e_{ij}^y(\mathbf{v}), \quad \beta = 1, 2, \\ \delta_\tau \varrho_{Y_2}(\mathbf{u}, \mathbf{v}) &= \oint_{Y_2} \rho_2 \mathbf{u} \cdot \mathbf{v} \nabla_y \cdot \vec{\mathbf{v}}, \\ \delta_\tau \langle \rho \rangle &= \rho^1 \oint_{Y_1} \nabla_y \cdot \vec{\mathbf{v}} + \rho^2 \oint_{Y_2} \nabla_y \cdot \vec{\mathbf{v}}, \end{aligned} \tag{39}$$

where  $\oint_{Y_\beta} = |Y|^{-1} \int_{Y_\beta}$ .

**Sensitivity of the effective elasticity  $\mathbb{D}$**  We can now differentiate the expressions for  $\mathbb{D}$  defined in (8a), to obtain  $\delta \mathbb{D}$ . This yields

$$\begin{aligned} \delta D_{ijkl} |Y| &= \delta_\tau a_{Y_1} \left( \mathbf{w}^{ij} + \mathbf{\Pi}^{ij}, \mathbf{w}^{kl} + \mathbf{\Pi}^{kl} \right) + a_{Y_1} \left( \delta_\tau \mathbf{\Pi}^{ij}, \mathbf{w}^{kl} + \mathbf{\Pi}^{kl} \right) + a_{Y_1} \left( \mathbf{w}^{ij} + \mathbf{\Pi}^{ij}, \delta_\tau \mathbf{\Pi}^{kl} \right) \\ &\quad + a_{Y_1} \left( \delta \mathbf{w}^{ij}, \mathbf{w}^{kl} + \mathbf{\Pi}^{kl} \right) + a_{Y_1} \left( \mathbf{w}^{ij} + \mathbf{\Pi}^{ij}, \delta \mathbf{w}^{kl} \right), \end{aligned}$$

where  $\delta_\tau \mathbf{\Pi}_k^{ij} = \mathcal{V}_j \delta_{ik}$ , see (8a). Note that  $\delta_t |Y| = 0$  due to the design parameterization. The last two integrals involving the undesired differentials  $\delta \mathbf{w}^{kl}, \delta \mathbf{w}^{ij}$  cancel due to (8b) evaluated for  $\mathbf{v} = \delta \mathbf{w}^{kl}$ , or  $\mathbf{v} = \delta \mathbf{w}^{ij}$ . Hence, using (39)<sub>1</sub>, we get the following explicit formula:

$$\begin{aligned} \delta D_{mnpq} &= \oint_{Y_\beta} C_{irks}^\beta \left( \delta_{rj} \delta_{sl} \nabla_y \cdot \vec{\mathbf{v}} - \delta_{jr} \partial_s^y \mathcal{V}_l - \delta_{ls} \partial_r^y \mathcal{V}_j \right) e_{kl}^y(\mathbf{w}^{mn} + \mathbf{\Pi}^{mn}) e_{ij}^y(\mathbf{w}^{pq} + \mathbf{\Pi}^{pq}) \\ &\quad + \oint_{Y_\beta} \left( C_{pjkl}^\beta e_{kl}^y(\mathbf{w}^{mn} + \mathbf{\Pi}^{mn}) \partial_j^y \mathcal{V}_q + C_{ijml}^\beta \partial_l^y \mathcal{V}_n e_{ij}^y(\mathbf{w}^{pq} + \mathbf{\Pi}^{pq}) \right). \end{aligned} \tag{40}$$



## Acknowledgement

E. Rohan and J. Heczko have been supported by the Czech Science Foundation through project No. P101/12/2315 and J. Vondřejc partially by the project EXLIZ – CZ.1.07/2.3.00/30.0013, which is co-financed by the European Social Fund and the state budget of the Czech Republic.

## References

- [1] M. S. Alnæs, A. Logg, K. B. Ølgaard, M. E. Rognes, and G. N. Wells. Unified Form Language: a Domain-Specific Language for Weak Formulations of Partial Differential Equations. *ACM Transactions on Mathematical Software*, 40(2), 2014.
- [2] J. L. Auriault and G. Bonnet. Dynamique des composites elastiques periodiques. *Arch. Mech.*, 37:269–284, 1985.
- [3] J. L. Auriault and C. Boutin. Long wavelength inner-resonance cut-off frequencies in elastic composite materials. *International Journal of Solids and Structures*, 49(23-24):3269–3281, 2012.
- [4] A. Ávila, G. Griso, B. Miara, and E. Rohan. Multiscale modeling of elastic waves: Theoretical justification and numerical simulation of band gaps. *Multiscale Modeling & Simulation, SIAM*, 7:1–21, 2008.
- [5] G. Bouchitté and D. Felbacq. Homogenization near resonances and artificial magnetism from dielectrics. *C.R.Acad.Sci, Math.*, 1339:377–382, 2004.
- [6] R. Cimrman and E. Rohan. Three-phase phononic materials. *Appl. Comp. Mech.*, 3:5–16, 2009.
- [7] R. Cimrman and E. Rohan. On acoustic band gaps in homogenized piezoelectric phononic materials. *Appl. Comp. Mech.*, 4:89–100, 2010.
- [8] D. Cioranescu, A. Damlamian, and G. Griso. The periodic unfolding method in homogenization. *SIAM Journal on Mathematical Analysis*, 40(4):1585–1620, 2008.
- [9] S. J. Cox and D. C. Dobson. Band structure optimization of two-dimensional photonic crystals in h-polarization. *Journal of Computational Physics*, 158(2):214–224, 2000.
- [10] H.-W. Dong, X.-X. Su, Y.-S. Wang, and C. Zhang. Topological optimization of two-dimensional phononic crystals based on the finite element method and genetic algorithm. *Struct. Multidiscip. Optim.*, 50(4):593–604, Oct. 2014.
- [11] H. W. Dong, X. X. Su, Y. S. Wang, and C. Zhang. Topology optimization of two-dimensional asymmetrical phononic crystals. *Physics Letters A*, 378:434–441, 2014.
- [12] Z. fa Liu, B. Wu, and C. fu He. Band-gap optimization of two-dimensional phononic crystals based on genetic algorithm and fpwe. *Waves in Random and Complex Media*, 24(3):286–305, 2014.
- [13] M. Farhat, S. Guenneau, S. Enoch, and A. B. Movchan. Negative refraction, surface modes, and superlensing effect via homogenization near resonances for a finite array of split-ring resonators. *Physical Review E - Statistical, Nonlinear, and Soft Matter Physics*, 80(4), 2009.



- [14] C. Geuzaine and J.-F. Remacle. Gmsh: A 3-D finite element mesh generator with built-in pre- and post-processing facilities. *International Journal for Numerical Methods in Engineering*, 79(11):1309–1331, 2009.
- [15] J. Haslinger and R. A. E. Mäkinen. Introduction to shape optimization. *Advances in Design and Control*, SIAM, 2003.
- [16] J. Haslinger and P. Neittaanmäki. *Finite Element Approximation for Optimal Shape Design*. J. Wiley, Chichester, 1988.
- [17] E. J. Haug, K. Choi, and V. Komkov. *Design Sensitivity Analysis of Structural Systems*. Academic Press, Orlando, 1986.
- [18] B. Henderson, K. Maslov, and V. Kinra. Experimental investigation of acoustic band structures in tetragonal periodic particulate composite structures. *J. Mech. Phys. Solids*, 49:2369–2383, 2001.
- [19] J. S. Jensen and N. L. Pedersen. On maximal eigenfrequency separation in two-material structures: The 1d and 2d scalar cases. *Journal of Sound and Vibration*, 289:967–986, 2006.
- [20] D. Kraft. A software package for sequential quadratic programming, 1988.
- [21] A. Krushynska, V. Kouznetsova, and M. Geers. Towards optimal design of locally resonant acoustic metamaterials. *Journal of the Mechanics and Physics of Solids*, 71:179–196, nov 2014.
- [22] V. Laude. *Phononic Crystals: Artificial Crystals for Sonic, Acoustic, and Elastic Waves*. Walter de Gruyter GmbH & Co KG, 2015.
- [23] A. Logg, K.-A. Mardal, and G. Wells, editors. *Automated Solution of Differential Equations by the Finite Element Method: The FEniCS book*. Lecture Notes in Computational Science and Engineering. Springer, Berlin, Heidelberg, 2012.
- [24] A. Madeo, P. Neff, I. Ghiba, L. Placidi, and G. Rosi. Wave propagation in relaxed micromorphic continua: modeling metamaterials with frequency band-gaps. *Continuum Mechanics and Thermodynamics*, 27(4-5):551–570, 2015.
- [25] H. Men, N. Nguyen, R. Freund, P. Parrilo, and J. Peraire. Bandgap optimization of two-dimensional photonic crystals using semidefinite programming and subspace methods. *Journal of Computational Physics*, 229:3706–3725, 2010.
- [26] H. Men, N. C. Nguyen, R. M. Freund, and K. M. Lim. Design of photonic crystals with multiple and combined band gaps. *Physical Review E*, 83(4), 2011.
- [27] B. Miara and E. Rohan. Homogenization and shape sensitivity of microstructures for design of piezoelectric bio-materials. *Mechanics of Advanced Materials and Structures*, 13:473–485, 2006.
- [28] B. Miara, E. Rohan, M. Zidi, and B. Labat. Piezomaterials for bone regeneration design – homogenization approach. *Jour. of the Mech. and Phys. of Solids*, 53:2529–2556, 2005.
- [29] G. Milton and J. Willis. On modifications of newton’s second law and linear continuum elastodynamics. *Proc. R. Soc. A*, 483:855–880, 2007.

- [30] J. H. Park, P. S. Ma, and Y. Y. Kim. Design of phononic crystals for self-collimation of elastic waves using topology optimization method. *Structural and Multidisciplinary Optimization*, 51(6):1199–1209, dec 2014.
- [31] R. E. Perez, P. W. Jansen, and J. R. R. A. Martins. pyOpt: a Python-based object-oriented framework for nonlinear constrained optimization. *Structural and Multidisciplinary Optimization*, 45(1):101–118, may 2011.
- [32] K. Pham, V. Kouznetsova, and M. Geers. Transient computational homogenization for heterogeneous materials under dynamic excitation. *Journal of the Mechanics and Physics of Solids*, 61(11):2125–2146, nov 2013.
- [33] E. Rohan, R. Cimrman, and B. Miara. Modelling response of phononic Reissner-Mindlin plates using a spectral decomposition. *Applied Mathematics and Computation*, 258:617–630, 2015.
- [34] E. Rohan and B. Miara. Sensitivity analysis of acoustic wave propagation in strongly heterogeneous piezoelectric composite. In *Topics on Mathematics for Smart Systems*, pages 139–207. World Sci. Publishing Company, 2006.
- [35] E. Rohan and B. Miara. Shape sensitivity analysis for material optimization of homogenized piezo-phononic materials. In *Proceedings of the WCSMO-8, Lisbon, Portugal*, pages 1–10, 2009.
- [36] E. Rohan and B. Miara. Band gaps and vibration of strongly heterogeneous Reissner-Mindlin elastic plates. *Comptes Rendus Mathematique*, 349:777–781, 2011.
- [37] E. Rohan and B. Miara. Elastodynamics of strongly heterogeneous periodic plates using Reissner-Mindlin and Kirchhoff-Love models. *Z. angew. Math. Mech.*, 2015.
- [38] E. Rohan, B. Miara, and F. Seifrt. Numerical simulation of acoustic band gaps in homogenized elastic composites. *International Journal of Engineering Science*, 47:573–594, 2009.
- [39] E. Rohan, J. Vondřejc, and J. Heczko. Shape optimization for homogenized phononic materials and band gap structures. In H. Rodrigues, J. Herskovits, C. M. Soares, J. M. Guedes, A. Araujo, J. Folgado, F. Moleiro, and J. A. Madeira, editors, *Proceedings of the International Conference on Engineering Optimization (EngOpt 2014)*, London, UK, 2015. CRC Press/Balkema.
- [40] F. Schury, M. Stingl, and F. Wein. Slope constrained material design. *Structural and Multidisciplinary Optimization*, 46(6):813–827, may 2012.
- [41] O. Sigmund and J. S. Jensen. Systematic design of phononic band-gap materials and structures by topology optimization. *Philosophical transactions. Series A, Mathematical, physical, and engineering sciences*, 361(1806):1001–19, may 2003.
- [42] V. P. Smyshlyaev. Propagation and localization of elastic waves in highly anisotropic periodic composites via two-scale homogenization. *Mechanics of Materials*, 41:434–447, 2009.
- [43] J. Vasseur, P. Deymier, G. Frantzikonis, G. Hong, B. Djafari-Rouhani, and L. Dobrzynski. Experimental evidence for the existence of absolute acoustic band gaps in two-dimensional periodic composite media. *J. Phy. Condens. Matter*, 10:6051–6064, 1998.
- [44] S. L. Vatanabe, G. H. Paulino, and E. C. N. Silva. Maximizing phononic band gaps in piezo-composite materials by means of topology optimization. *J. Acoust. Soc. Am.*, 136:494–501, 2014.

- [45] J. Vondřejc, J. Zeman, and I. Marek. An FFT-based Galerkin method for homogenization of periodic media. *Computers & Mathematics with Applications*, 68(3):156–173, aug 2014.
- [46] J. Vondřejc, J. Zeman, and I. Marek. Guaranteed upper-lower bounds on homogenized properties by FFT-based Galerkin method. *Computer Methods in Applied Mechanics and Engineering*, 297:258–291, 2015.
- [47] A. Wächter and L. Biegler. On the implementation of an interior-point filter line-search algorithm for large-scale nonlinear programming. *Mathematical programming*, 106(1):25–57, 2006.
- [48] A. Wautier and B. B. Guzina. On the second-order homogenization of wave motion in periodic media and the sound of a chessboard. *Journal of the Mechanics and Physics of Solids*, 78:382–414, mar 2015.
- [49] E. Yablonovitch. Photonic band-gap crystals. *J. Phys. Condens. Matter*, 5:2443–2460, 1993.
- [50] O. Yuksel and C. Yilmaz. Shape optimization of phononic band gap structures incorporating inertial amplification mechanisms. *Journal of Sound and Vibration*, 355:232–245, jul 2015.